Journal of Cleaner Production 393 (2023) 136126

Contents lists available at ScienceDirect

Journal of Cleaner Production

journal homepage: www.elsevier.com/locate/jclepro

Selective adsorption of Pb (II) and Cu (II) on mercapto-functionalized aerogels: Experiments, DFT studies and LCA analysis

Yaoyao Zhang [a,b,c], Kangze Yuan [d,***], Luca Magagnin [c,**], Xishe Wu [b], Zhenyi Jiang [e], Wei Wang [a,b,*]

[a] Key Laboratory of Subsurface Hydrology and Ecological Effects in Arid Region of the Ministry of Education, Chang'an University, Xi'an, Shaanxi, 710054, PR China
[b] School of Water and Environment, Chang'an University, Xi'an, Shaanxi, 710054, PR China
[c] Department of Chemistry, Materials and Chemical Engineering "Giulio Natta", Politecnico di Milano, via Mancinelli 7, 20131, Milano, Italy
[d] College of Geological Engineering and Geomatics, Chang'an University, Xi'an, Shaanxi, 710054, PR China
[e] Institute of Modern Physics, Northwest University, Xi'an, Shaanxi, 710054, PR China

ARTICLE INFO

Handling Editor: Zhen Leng

Keywords:
Mercaptan functional group
Heavy metals
Mechanism
DFT
LCA

ABSTRACT

Mercapto-functionalized aerogels (MA-X) were fabricated using γ-mercaptopropyltrimethoxysilane (MPTMS) as a modification reagent to eliminate Pb (II) and Cu (II) ions from wastewater. Mercapto-functionalized aerogel (MA2) with the MPTMS/TEOS molar ratio of 0.5 exhibited the maximum adsorption amounts of 163.99 mg/g for Pb (II) and 172.41 mg/g for Cu (II) in single ion system, respectively. In binary ion system, selective adsorption experiments revealed that the equilibrium adsorption capacity for Cu (II) (161.29 mg/g) was significantly greater than Pb (II) (90.42 mg/g), and the selectivity factor α showed greater selectivity for Cu (II), demonstrating that Cu (II) was more readily adsorbed on MA2. The results showed that adsorption was consistent with pseudo-second order model and Langmuir model. Thermodynamic results demonstrated that adsorption phenomenon was an exothermic reaction that occurred spontaneously. XPS analysis and density functional theory (DFT) simulations showed that the main mechanism for the adsorption of Pb (II) and Cu (II) on MA2 was through coordination chelation of the –SH groups with Pb (II) and Cu (II). DFT calculations showed a lower adsorption energy (E_{ads}) of Cu (II) (−2.72 eV) with respect to Pb (II) (−0.80 eV), indicating that Cu (II) was more stably adsorbed on MA2 and more difficult to exchange by Pb (II). In order to determine the environmental impact of the MA2 preparation process, a life cycle assessment (LCA) was conducted and contribution of each material to MA2 production was analyzed. Finally, a strategy that is environmentally friendly and effective has been proposed in order to facilitate MA-X adsorbents production and to improve their application for the treatment of heavy metal polluted wastewater.

1. Introduction

The increase in industrial manufacture and socio-economic activities has not only raised the standard of living, but also produced wastewater containing heavy metal contamination (Chen et al., 2019). As one of the most hazardous heavy metals, a number of industrial activities related to Pb, such as leaded gasoline, lead battery manufacturing, lead pipe manufacturing, paint and pigment manufacturing, agrochemicals, lead mining, cosmetics, ceramic manufacturing, etc., all cause Pb pollution of the environment and thus enter the human body by the food chain (Kumar et al., 2022; Swaringen et al., 2022). Lead (II) adversely affects human systems and living organisms including nephrotoxicity, carcinogenicity and cardiovascular toxicity (Mitra et al., 2022). Some world organizations set a tolerance of 15 and 10 μg/L for Pb (II) in drinking water, respectively (Awual, 2019a, 2019b). Therefore, it is critical to human health and environmental safety to enhance removing Pb (II) ions from wastewater.

Unlike lead, copper is exceptional since it is both a micronutrient for

* Corresponding author. Key Laboratory of Subsurface Hydrology and Ecological Effects in Arid Region of the Ministry of Education, Chang'an University, Xi'an, Shaanxi, 710054, PR China.
** Corresponding author.
*** Corresponding author.
E-mail addresses: yuan135830@126.com (K. Yuan), luca.magagnin@polimi.it (L. Magagnin), wwchem@126.com (W. Wang).

https://doi.org/10.1016/j.jclepro.2023.136126
Received 10 October 2022; Received in revised form 9 January 2023; Accepted 18 January 2023
Available online 3 February 2023

living organisms and an element of environmental pollution (Li et al., 2020). The maximum tolerable range for Cu (II) is 1.0–2.0 mg/L in drinking water according to the USEPA and WHO (Katiyar et al., 2021). The human body cannot produce copper and therefore it needs to be obtained from the diet. The World Health Organization declares that the body needs small intakes of copper to protect against any symptoms of deficiency. However, it is rare that adults may develop such a deficiency (Rehman et al., 2019). Excessive intake of copper may be associated with severe toxicological issues such as gastrointestinal distress, stomach cramps, nausea, vomiting, convulsions and diarrhoea. It is mainly found in the liver, muscles and bones where it accumulates in these organs, resulting in the most typical case known as Wilson's disease (Krstić et al., 2018; Kumar et al., 2021). Therefore, there is a strong necessity to find an effective treatment for Cu-containing wastewater (Wang et al., 2019).

In order to eliminate those heavy metal ions from waste water, many techniques are adopted including photocatalysis degradation, membrane filtration, ion-exchange, flocculation, chemical precipitation, electrochemical treatment and adsorption (Hossaini-Zahed et al., 2022; Tang et al., 2020). Among these methods, adsorption is of growing concern owing to its operational simplicity, high efficiency and selectivity, recyclability and low cost (Wang et al., 2019; Ghaedi et al., 2018). In recent years, a variety of low-cost materials such as industrial by-products, mineral deposits, naturally occurring soils, agricultural waste, and other available waste materials have been used as sorbents (Krstić et al., 2018; Joseph et al., 2019). However, there are limitations to the use of these absorbents and to overcome these shortcomings, high efficiency adsorbents possessing tailored functionalized groups, high porosity, large specific surface area and mild preparation conditions are urgently needed (Ghaedi et al., 2018).

It is well known that mercaptan groups are always involved to improve the removal of heavy metal ions. For example, Li et al. (2015) synthesized chitosan/sulfydryl-functionalized graphene oxide composite (CS/GO-SH), which exhibited excellent performance toward Cd (II), Pb (II) and Cu (II) with 177 mg/g, 447 mg/g and 425 mg/g, respectively. Thiol-functionalized graphene oxide (GO-SH) was prepared by Nuengmatcha et al. (2015), and it was found to be effective in removing Hg (II) from aqueous solutions, indicating that thiol-modified graphene oxide may act as a promising sorbent towards toxic metals. Han et al. (2015) investigated mercapto functionalized palygorskite (MPAL) for the removal of Cu (II) from aqueous solutions. The results showed that the complexation of the mercapto functional group of MPAL with Cu (II) played an important role in the adsorption process, and the maximum adsorption of Cu (II) was increased by 10 times compared to the original palygorskite. The sulfhydryl functionalization of magnetic graphene quantum dots (Fe_2O_3-GQDs-SH, FGM) enabled rapid and efficient adsorption of Cd (II), where the sulfhydryl group made a significant contribution in the adsorption process (Nuengmatcha, 2021). Meanwhile, there has been much interest in porous materials due to the availability of more binding sites (Mirzaee et al., 2019). Notably, silica-based aerogels have many special properties including high specific surface area and high porosity (Sert Çok et al., 2021). These properties are essential for an excellent adsorbent. Numerous studies have been reported on the application of silica-based aerogels for the adsorption of a variety of different types of pollutants. For instance, Yang et al. (2021) achieved efficient removal of phosphate using lanthanum-modified mesoporous silica aerogels by freeze-drying methods. Liu et al. (2021) prepared methyl acrylate modified silica aerogel (TEPA-MA-SA) by CO_2 supercritical drying, which can efficiently adsorb Cu (II) from aqueous solutions and is deemed to be an assisted adsorbent for the purification of wastewater. Vareda and Durães (2019) prepared amine-, mercapto-functionalized silica aerogel adsorbents for the adsorption of Cu (II), Pb (II), Cd (II), Ni (II), Cr (II) and Zn (II) from watercourses and groundwater, demonstrating that sol-gel method is an excellent way to provide the synthesis of materials with tailored surface chemical functionality. Ehgartner et al. (2021) developed organofunctionalized methyltrimethoxy (MTMS) aerogels by a facile sol-gel method for the selective adsorption of heavy metal cations, allowing them to be ideal adsorbent candidates. Furthermore, the modification of the chemical properties of the silica aerogels by the introduction of organic functional groups is one of its most valuable properties (Štandeker et al., 2011). However, most reported aerogels are prepared by supercritical drying or freeze-drying processes, which are both high-cost and time-consuming, whereas ambient pressure drying is a low-cost and more efficient method for large-scale production of aerogels (Ganesamoorthy et al., 2021). Therefore, a combination of mercapto groups and aerogels to design an environmentally friendly and cost-effective synthesis process with tailored high-efficiency functional aerogel materials for the removal of heavy metal ions from water appears to be of essential importance.

The explanation of the adsorption mechanism is largely by experimental trials, characterization and classical models, is not sufficiently accurate (Abdel-Magied et al., 2022; Cao et al., 2022). In recent years, the introduction of density functional theory (DFT) calculations seems to have solved this problem. DFT simulates realistically the thermodynamic properties of fluids within porous materials by using molecular dynamics. And it has been developed as a robust technique for predicting the structure of new materials, and widely applied for understanding the adsorption mechanism at the atomic level microscopic standpoint (Xu et al., 2021; Chen et al., 2022). As the global economy grows rapidly, there is increasing attention to environmental sustainability. Despite that aerogels present a prospective future for the removal of heavy metal ions, there are still many issues, including technical issues, economic costs and environmental impacts, the first and foremost of which is to consider the impact of the production of aerogels on the public environment and human health, which can help aerogel materials in the markets (Franco et al., 2021). Therefore, the life cycle assessment (LCA) was introduced to analyze the environment impact of aerogels in this study. LCA can analyze the environmental and health impacts of products, services, and assets through reduction of emissions, consumption of resources, and associated costs (ILCD 2010). Previous applications include people's lives and construction. Recently, LCA has been involved in the field of absorbents and has made progress in the development of a number of international standards (Gupta and Suhas, 2009). However, there are still few reported studies on the introduction of LCA into sorbents for the adsorption of heavy metal ions.

Herein, we explored a straightforward sol-gel method to prepare mercapto-functionalized silica aerogels by atmospheric pressure drying using TEOS and MPTMS as co-precursors. The main objectives of this work were: (1) to systematically characterize the new prepared adsorbents; (2) to assess the adsorption properties for Pb (II) and Cu (II); (3) to unveil the selective adsorption mechanism of MA2 on Pb (II) and Cu (II) by DFT calculation studies from the atomic level perspective; (4) to investigate the impact of the adsorbent production process on the environment and public health using a life cycle assessment.

2. Material and methods

2.1. Materials

Tetraethoxysilane (TEOS), ethanol (ETOH), hydrochloric acid (HCl), ammonia (NH_4OH), n-Hexane, lead chloride ($PbCl_2$), Copper chloride ($CuCl_2$), were acquired by Xian Chemical Reagent Co. Ltd. γ-mercaptopropyltrimethoxysilane (MPTMS) was offered by Shanghai Aladdin Biochemical Technology Co. Ltd.

2.2. Preparation of mercapto-functionalized silica aerogels (MA-X)

Silica gels were synthesized using TEOS and MPTMS as co-silica sources with the sol-gel method, TEOS was dissolved in ethanol, and MPTMS solution was gradually added under stirring. The pH of the solution was set to 3 by adding 0.1M HCl (all water was displaced by 0.1M

HCl), stirred and heated to 60 °C for 2 h, then 3 mL of 1 mol/L ammonia was added to the solution with vigorous stirring for 1–2 min and transferred to the mold for gelation. After gel formation, the gels were aged in ethanol for 24 h in a water bath at 40 °C, then exchanged 6 times with ethanol during 48 h for removing surplus water and excess organic solvents, followed by 4 times over 48 h with n-hexane. Finally, the mercapto-functionalized aerogels (MA-X) were fabricated by atmospheric pressure drying (APD) at 40 °C and 60 °C for 48 h and 24 h respectively. The samples were labeled MA1, MA2, MA3 and MA4 depending on the molar ratio of MPTMS: TEOS ranging from 0.3, 0.5, 0.7 to 1.0. The molar ratios of n(TEOS): n(ETOH): n(H_2O) was 1 : 10: 16. The flowchart for preparation of mercapto-functionalized aerogels was shown in Fig. 1. MA2 was used for DFT calculations and LCA analysis due to its optimal performance for Pb (II) and Cu (II) adsorption.

2.3. Characterizations

The microscopic morphology was studied on a Scanning Electron Microscopy (SEM, Hitachi S-4800, Japan). The surfaces of aerogels were analyzed with Fourier Transform Infrared spectrometers (Nicolet 5700). XRD was applied to identify the phase-composition of the samples using an X-Ray diffractometer (D8 ADVANCE). The specific surface area and porous structure were characterized with a NOVA 2200 analyzer (BET, Quantachrome, US). The zeta potential of the adsorbents was measured by a zeta potential measurement (Malvern Instruments, UK) at different pH values and a Setaram Labsys Evo instrument was used to preform thermogravimetric analysis (TGA). Aerogel chemical binding states were determined before and after adsorption using X-ray photoelectron spectroscopy (XPS, ESCALAB 250, USA). With an Elemental Analyzer (Elementar Vario EL Cube, Germany), the samples were measured for elemental content. The concentrations of Pb (II) and Cu (II) were determined by atomic absorption spectrophotometry (AAS, WFX-120, Beijing Rayleigh Analytical Instrument Co., Ltd.).

2.4. Adsorption experiments

A single and binary metal ion system using 1.0 g/L adsorbent has been performed using 50 mg/L Pb (II) and 50 mg/L Cu (II) solutions in 50 mL centrifuge tubes. The influences of pH on Pb (II) and Cu (II) adsorption were evaluated by varying the initial pH from 1 to 6 with 0.1 M NaOH and 0.1 M HCl solutions. To investigate the kinetics, 20 mg MA2 and 20 mL of different concentrations (50–200 mg/L) of Pb (II) and Cu (II) solutions were adsorbed at 298 K for a specific time in single metal ion system and 10 mL 100 mg/L Pb (II) and 10 mL 100 mg/L Cu (II) solution were tested using 20 mg adsorbent in binary metal ion system. Isotherm experiments were performed in different initial concentration varied from 50 mg/L to 1000 mg/L in single metal ion system and 25 mg/L to 500 mg/L in binary metal ion system. Thermodynamics tests were also performed at different temperatures (293–318 K) at pH 5. Five consecutive adsorption-desorption cycles were carried out to assess the recyclability of the adsorbents. 25 mL 0.1 M HCl solution was added after each adsorption, stirred for 180 min, and then the next adsorption experiment was performed. Supplementary Material including more details of the isotherms, kinetics and thermodynamic equations associated with the adsorption model are presented in **Text S1**.

2.5. DFT calculation

The DFT calculations were performed by Gaussian 09 software (Frisch et al., 2009). The calculations were simulated with B3LYP functional group at the ground state (Sellaoui et al., 2019). In terms of geometrical optimization and frequency calculations, the LanL2DZ basis set was applied to Pb and Cu atoms, and the 6–31g(d) basis set was used for other atoms. The singlet point energy calculation was employed with the LanL2DZ basis set for Pb and Cu atoms, and 6–311 g(d, p) for other atoms (Ji et al., 2022; Wang et al., 2013). To take solvation effects into account, the DFT computations adopted the Integral Equation Formalism Polarized Continuum Model (IEFPCM) and water as the solvent (Zhang et al., 2021; Oyetade et al., 2017). The adsorption energy (E_{ads}) is calculated using Eq. (1) (Xu et al., 2021; Chen et al., 2022).

$$E_{ads} = E_{total} - (E_{adsorbent} + E_{metal}) \quad (1)$$

where E_{total} describes the total energy related to the adsorption of Pb (II) or Cu (II) onto MA2, $E_{adsorbent}$ refers to the energy of MA2 and E_{metal} implies the energy of individual heavy metal Pb or Cu atom, respectively.

2.6. Life cycle assessment (LCA)

2.6.1. Goal and scope definition

The environmental footprint of any product can be assessed throughout its life cycle by means of a Life Cycle Assessment (LCA). This study was carried out using the LCA method to characterize and assess the environmental impacts involved in the production of 1 kg of mercapto-functionalized aerogel (MA2). The software package used to calculate the impacts was eFootprint and the method was based on the guidelines from ISO 14044 standard. Environmental hotspots were identified in MA2 production by analyzing the contribution of each material, and additional strategies to mitigate negative impacts on sustainability were proposed.

Fig. 2 provide the system boundaries for a cradle-to-grave LCA, which includes the production, transportation, and preparation of raw materials that make up the MA2. Raw material transport distances were

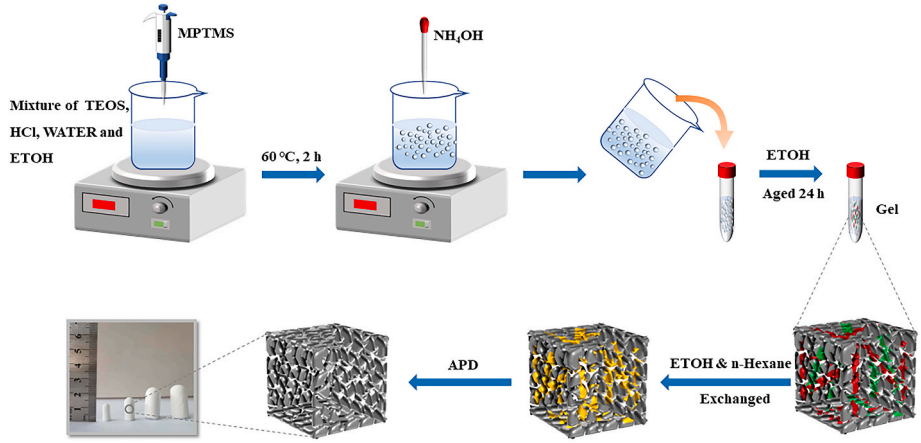

Fig. 1. Flowchart for preparation of mercapto-functionalized aerogels.

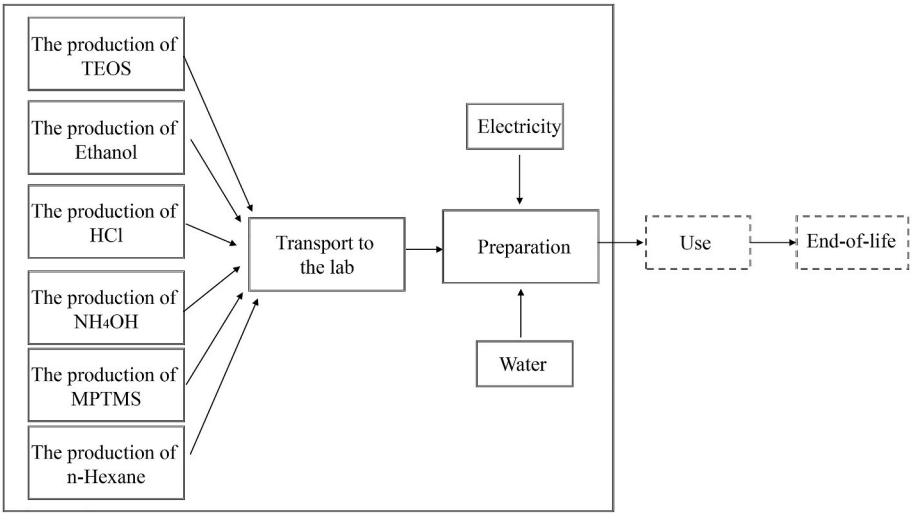

Fig. 2. MA2 adsorbent production schematic diagram from cradle to grave.

calculated based on China's average distance of 181 km. As there is not environmental impact during the use phase, disposal is not required during the end-of-life phase. This work does not take into account the use and end-of-life phases.

2.6.2. Life cycle inventory analysis

Life Cycle Inventory (LCI) analysis is the second stage of LCA research. It is responsible for collecting data about all inputs and outputs recognized at the boundaries of a system. As described in section 2.2 and previous literature, the inventory was compiled and recorded based on the above boundary. EFootprint was used for calculations, and Ecoinvent database v.3.1 and CLCD were used to access all LCI data. The work assumed that production would be powered by a global average electricity mix. The LCI of MA2 is shown in Table 1.

2.6.3. Life cycle impact assessment

According to Ferrão (2009), assessing environmental impacts must be linked to choosing a method of evaluation. In this study, the method used was based on intermediate indicators focusing on environmental loads and final consequences. The CML 2001 method was used, with categories such as: Global Warming Potential (GWP), Acidification Potential (AP), Abiotic Depletion Potential (ADP), Eutrophication Potential (EP), Ozone Depletion Potential (ODP), and Photochemical Ozone Creation Potential (POFP). Meanwhile, a category for Primary Energy Demand (PED) has been added, based on the Cumulative Energy Demand (CED) approach. Finally in this work, data quality assessments were carried out for each indicator, which allowed the uncertainty of the results and confidence intervals of 95% for the upper and lower ranges to be determined.

Table 1
Life Cycle Inventory for the production of 1 kg MA2.

	Mass	Unit
Raw material input		
TEOS	0.94	kg
Ethanol	46	kg
HCl	15.15	g
NH_3	5.1	g
MPTMS	86.15	g
n-Hexane	36.96	kg
Water	1.287	kg
Energy input		
Electricity	2	kWh
Transportation	181	km
Output		
MA2	1	kg

3. Results and discussion

3.1. Materials preparation and characterization

Firstly, the mercaptan silica aerogel backbone structure was synthesized by hydrolytic condensation reactions of TEOS and MPTMS. Secondly, the silica gel was formed by adjusting the pH of the solution by ammonia. Finally, the aqueous solution in the gel was removed by solvent exchange and dried under ambient pressure condition to obtain the mercapto-functionalized aerogels (MA-X) (Fig. 1). This new adsorbent should be able to have good adsorption properties by combining both Pb (II) and Cu (II).

Fig. 3a displayed the FTIR spectra of MA-X. The broad absorption peaks at about 3450 cm^{-1} and 1600 cm^{-1} are assigned to the characteristic peak of –OH. The peak at 543 cm^{-1}, 773 cm^{-1} and 1124 cm^{-1} correspond to Si–O bending vibration peak, symmetric vibration peak and asymmetric vibration peak, respectively. The absorption band at 2830 cm^{-1} and 1350 cm^{-1} are ascribed to the stretching vibrations of C–H and $–CH_2$, respectively (Liang et al., 2022). The peak appeared at 2580 cm^{-1} that corresponded to the –SH group, which proved a successful synthesis of MA-X (Naat et al., 2021). Furthermore, the elemental analysis results of MA1, MA2, MA3 and MA4 (containing 7.774%, 11.592%, 14.304% and 16.153% S, respectively) indicated that –SH was successfully introduced into the skeleton (Table S1). In addition, Fig. 3b showed the XRD patterns of MA-X. By comparison, the four samples were found to have similar diffraction peaks at around 22°, corresponding to the typical amorphous silica structure, suggesting that the hydrolysis and condensation reactions of TEOS are favoured for the formation of the amorphous structure (Chen et al., 2021). As the MPTMS/TEOS molar ratio increases, the diffraction intensity of the amorphous silica gradually decreases, demonstrating that the intervention of MPTMS reduces the relative crystallinity of silica aerogels (Zhu et al., 2021).

Fig. 4 showed that the morphology of the MA-X samples. It was found that a change was observed in increasing the molar ratio MPTMS/TEOS, namely the particles of the samples grew gradually. When the MPTMS/TEOS molar ratio was 0.3, the sample shrank more severely, resulting in an inhomogeneous surface. At a molar ratio of 0.5 for MPTMS/TEOS, it was observed that the surface pores of MA2 were evenly distributed and relatively coarse, which provided greater feasibility for heavy metal ion adsorption. With a further increase in the MPTMS/TEOS molar ratio, the MA3 and MA4 sample particles gradually grew larger and the surfaces

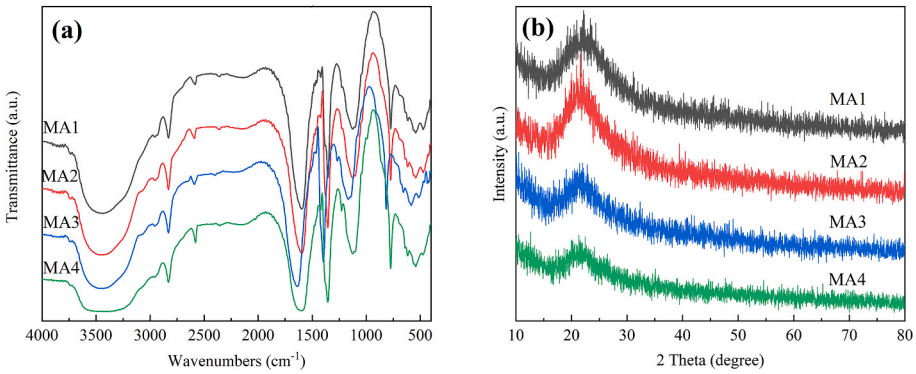

Fig. 3. FTIR spectra (a) and XRD patterns (b) of mercapto-functionalized aerogels.

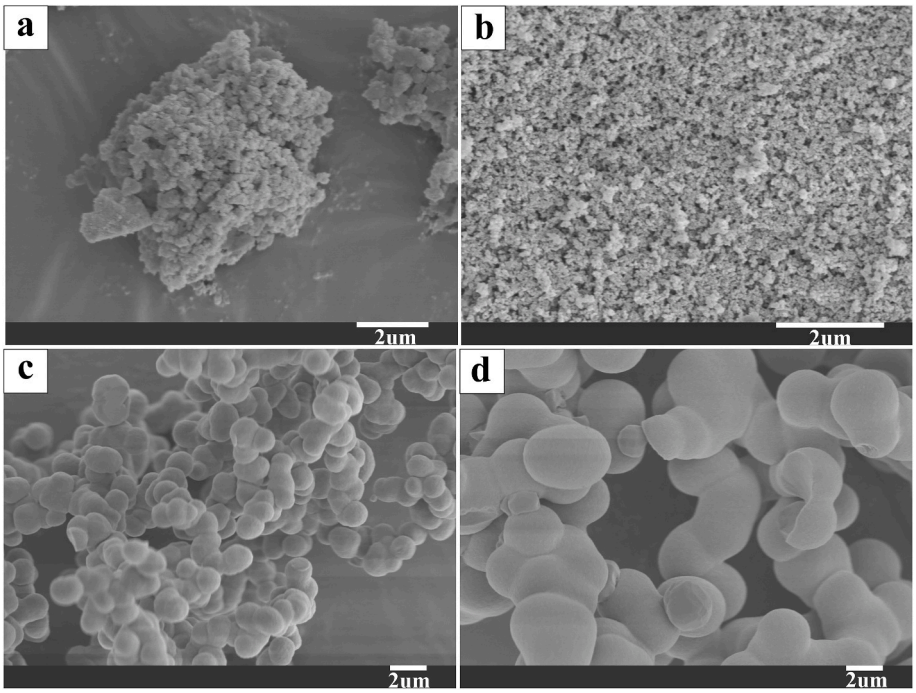

Fig. 4. SEM images of mercapto-functionalized aerogels. (a) MA1, (b) MA2, (c) MA3 and (d) MA4.

became smoother. This is because the co-hydrolysis processes of MPTMS and TEOS were carried out successively, leading to different microstructures. For these reasons, the MA-X samples become progressively less compact and more brittle.

As illustrated in Fig. 5, the N_2 adsorption-desorption isotherms for all samples of MA-X showed a type IV isotherm, implying a typical feature of mesoporous materials (Sert Çok et al., 2021; Yang et al., 2021). The specific surface areas of MA1, MA2, MA3 and MA4 were calculated to be 395.22 m^2/g, 341.78 m^2/g, 216.41 m^2/g and 172.62 m^2/g, respectively. And the pore size of MA1, MA2, MA3 and MA4 were 3.73 nm, 10.97 nm, 17.86 nm and 25.23 nm, respectively. There is only a small change in the specific surface area and pore size of MA2 compared to MA1, which is probably due to the increased MPTMS/TEOS ratio that occupies some of the surface and pore space. Further increasing the ratio of MPTMS/TEOS led to a considerable decrease in specific surface area, visible agglomeration of particles and an increase in particle size, which was unfavorable for the adsorption of heavy metal ions. The results confirmed that MPTMS had successfully been grafted onto aerogels skeleton, which aligned with observations from SEM imaging.

In addition, thermogravimetric analysis of MA1, MA2, MA3 and MA4 at 30–900 °C were investigated as presented in Fig. S1. It is apparent that there are minimal weight losses when the temperature is below 200 °C, which are mainly connected to the loss of water from physical adsorption in the pores (Štandeker et al., 2011). Then, the weight losses for MA1, MA2, MA3 and MA4 between 200 and 600 °C were observed to be 28.08%, 31.92%, 28.48% and 33.21%, respectively. These can be ascribed to the degradation of the –SH functional groups and organic components (Ecer et al., 2018; Lyu et al., 2020). There was no significant weight loss to be observed at temperatures above 600 °C, with weight losses of 3.55%, 2.63%, 3.76% and 2.72% for MA1, MA2, MA3 and MA4, respectively. From 200 °C the mercaptopropyl starts to decompose, with a sharp mass loss at around 400 °C for the decomposition of the mercapto group, the degradation being completed at around 600 °C (Hüsing and Schubert, 1997; Motahari et al., 2015). The total mass loss of MA1, MA2, MA3 and MA4 were 36.13%, 37.37%, 39.32 and 41.02%, respectively.

3.2. Heavy metal ion removal capacity

3.2.1. Comparison of adsorption capacity

Aerogels (MA-X) were obtained via the use of different molar ratios of MPTMS and TEOS precursors during the sol-gel synthesis. Fig. 6

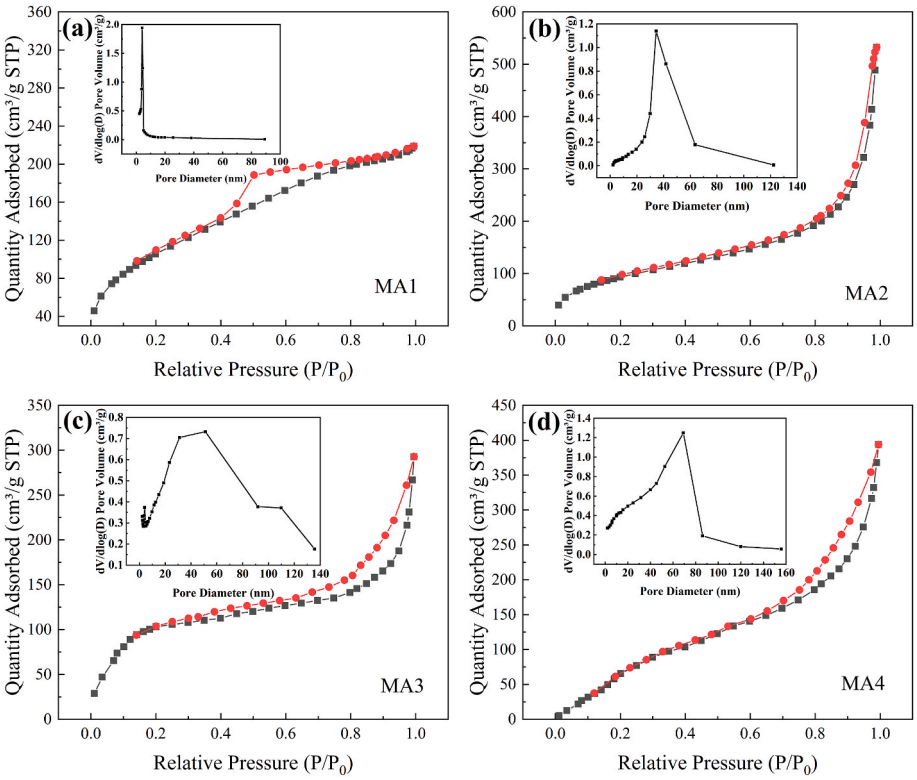

Fig. 5. N_2 adsorption-desorption isotherms and BJH pore size distribution of mercapto-functionalized aerogels.

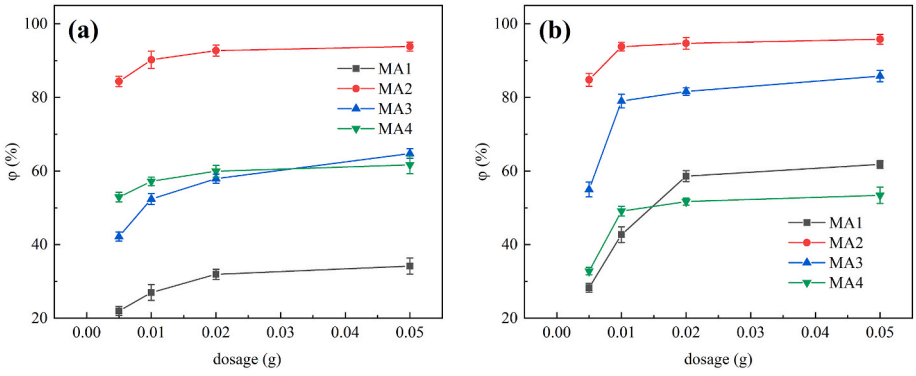

Fig. 6. Effect of different MPTMS/TEOS molar ratios on heavy metal ion adsorption. (a) Pb (II), (b) Cu (II).

shows that the MA2 aerogel has the optimal removal properties for both Pb (II) and Cu (II) at a molar ratio of 0.5 for MPTMS/TEOS. On the one hand, as the molar ratio increases, the aerogels particles get larger, become less compact and more brittle, and the pores will collapse more easily. On the other hand, as the MPTMS/TEOS molar ratio increases, mercapto aerogels may be obtained with a larger number of functional groups. However, owing to the reduced surface area and the aggregation of particles, these functional groups are not accessible to metal ions

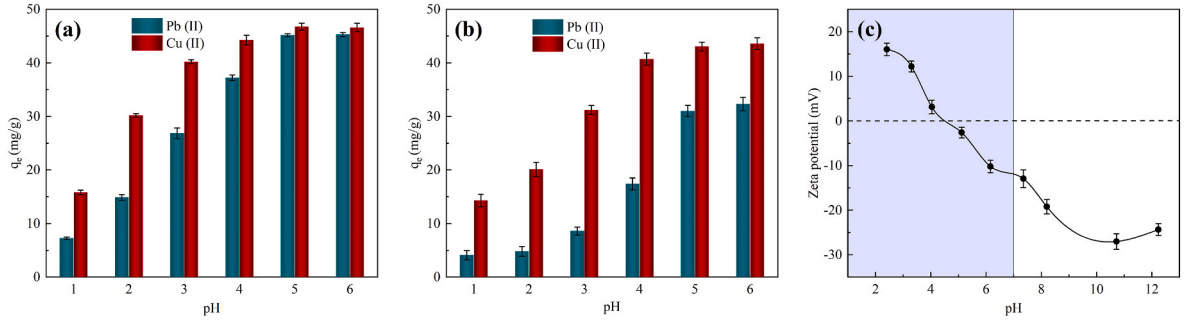

Fig. 7. pH influence on the adsorption of Pb (II) and Cu (II) by MA2 under (a) mono- and (b) bi-heavy metal ion system, (c) Zeta potential of MA2.

(Štandeker et al., 2011). MA2 was then chosen for subsequent studies on the adsorption of heavy metal ions.

3.2.2. Effect of pH

As to evaluate the adsorption performance for materials, the acidity of the solution has a strong influence with respect to the adsorption capacity of the material via the influence on the surface charge and solution chemistry (Ihsanullah et al., 2022; Zhu et al., 2022). Taking into account the precipitation behavior of Pb (II) and Cu (II), the adsorption process was conducted at a pH of 1.0–6.0. Fig. 7 showed the adsorption capacity increased with pH values from 1.0 to 5.0, and then remained at a relatively high value at pH 5.0 in single and binary heavy metal ion systems. In highly acidic media, there is in the case of acidic protons and metal ions competition for available alkaline sites (Betiha et al., 2020). Furthermore, the removal of metal ions is low at low pH values owing to the extensive electrostatic repulsion existing amongst the adsorbent and the metal ions (Heidari et al., 2018). As the increase of pH, the competition of protons and metal ions at alkaline sites decreases and the negative charge of MA2 surface increases, which facilitates the adsorption of metal ions and therefore increases the adsorption capacity. Apparently, Cu (II) was significantly more easily adsorbed onto MA2 than Pb (II) in the binary heavy metal ion system. The zeta potential results showed that MA2 became increasingly negative as the pH values of the suspension increased, and the point of zero charge (pH_{pzc}) of MA2 was 4.5 and a net negative charge presented at solution pH > 4.5. The negative potential facilitates to remove metal ions (Liang et al., 2013; Ihsanullah et al., 2022). In subsequent experiments, the optimal pH value was chosen at 5.

3.2.3. Adsorption kinetics

Adsorption is a complicated phenomenon involving a transferred process of adsorbate from liquid to solid phase, and potential chemical or physical interactions that may occur with the adsorbate and the adsorbent. Investigation of adsorption kinetics could reveal a lot of important parameters about the mechanism of adsorption. The experimental data are considered for simulation using Pseudo first order (Lagergren, 1898), Pseudo second order (Blanchard et al., 1984), Elovich (Roginsky and Zeldovich, 1934) and Intraparticle diffusion (Weber Jr and Morris, 1963) models.

As shown in Fig. 8, in both the single and binary systems, the adsorption of Cu (II) had a rapid increase within 20 min and reached equilibrium around 180 min, while the adsorption of Pb (II) was a slow process, achieving adsorption equilibrium after 360 min. This is probably ascribed to the considerable –SH groups on the MA2 surface during the initial reaction time. Interestingly, MA2 showed a high affinity toward Cu (II) and a comparatively low affinity toward Pb (II) in the binary system (Fan et al., 2020).

The non-linear fitted curves for these kinetic models are shown in Figs. S2–S3, and Table 2 lists the kinetic constants from the fitted data using non-linear regression analysis. Compared with the pseudo-first-order model, the pseudo-second-order model was found to give high correlation coefficient R^2, and the equilibrium adsorption (q_{cal}) calculated by the pseudo-second-order model were more closely matched experimental data (q_{exp}), further demonstrating the feasibility of the equation. Moreover, the Elovich equation can also describe the adsorption process well because of the higher R^2 values ($R^2 > 0.97$). Notably, the intraparticle diffusion diagram is composed of multiple linear sections, which means the adsorption process involves multiple steps (Tran et al., 2017). From Table 2, the intraparticle diffusion rate constant k_{p1} for the adsorption of Cu (II) by MA2 was found to be from 10.4754 to 21.0901, while MA2 for Pb (II) (3.1126–8.8114). The larger initial adsorption rate for Cu (II) compared to Pb (II) indicates a faster adsorption rate at the initial stage and faster adsorption by MA2 for Cu (II) than Pb (II) (Cheng et al., 2021).

3.2.4. Adsorption isotherm

To explore the possible maximum adsorption capacity of MA2, different initial concentrations of Pb (II) and Cu (II) were evaluated in single and binary systems (Fig. 9). A gradual increase in adsorption capacity is achieved with increasing initial concentrations of Pb (II) and Cu (II) until saturation is reached. A gradient of high concentration differences is responsible for the metal ions being adsorbed onto the adsorbent at an accelerated rate until the adsorption sites are completely occupied, thus reaching adsorption equilibrium (Tang et al., 2021). Also, in the binary competitive adsorption system, MA2 shows a greater affinity for Cu (II) than for Pb (II), indicating that MA2 is more favorable for Cu (II) adsorption.

Four adsorption isotherm models of Langmuir (1918), Freundlich (1906), Temkin (Tempkin and Pyzhev, 1940), and Dubinin-Radushkevich (D-R) (Dubinin, 1947) models are used to interpret Pb (II) and Cu (II) adsorption on MA2. Figs. S4–S5 depicted the non-linear fitted curves for the four model isotherms at different temperatures. As demonstrated in Table 3, the Langmuir model is more suitable for fitting the experimental data than other models with a higher correlation coefficient ($R^2 > 0.96$), and the calculated theoretical maximum adsorption capacity are much closer to the experimental value, implying that the Pb (II) and Cu (II) adsorption on MA2 are monolayer adsorption (Alqadami et al., 2020). Furthermore, the values of the separation factor R_L for Pb (II) adsorption by MA2 were in the range of 0.015–0.241 and for Cu (II) from 0.011 to 0.285, indicating that MA2 is favorable for both Pb (II) and Cu (II) adsorption (Ibrahim et al., 2022). The Freundlich model shows that n values are greater than 0 and less than 1, which implies that the adsorbent is favorable for the adsorption of metal ions (Sun et al., 2022). In addition, the Temkin model is also showing high correlation coefficient (R^2) values for Pb (II) and Cu (II), suggesting that physisorption of metal ions occurs on the MA2 (Yadav et al., 2021).

In addition, Table 4 compared the MA2 adsorption performance with aerogels and other adsorbents reported in the literature. MA2 exhibited a higher adsorption capacity for Pb (II) and Cu (II) compared to the geopolymer-, graphene-based- and biochar-adsorbents, demonstrating that MA2 has greater potential for the removal of Pb (II) and Cu (II).

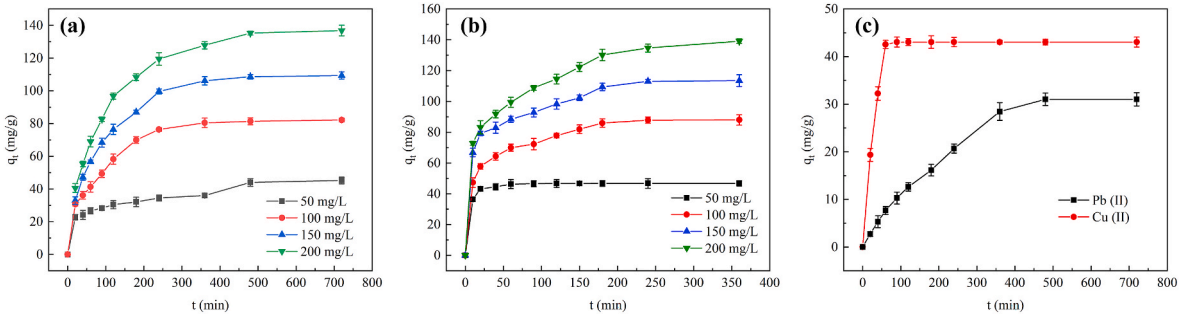

Fig. 8. Adsorption kinetic for the adsorption of Pb (II) (a) and Cu (II) (b) in single heavy metal ion system and Pb (II) and Cu (II) (c) in binary heavy metal ion system.

Table 2
Kinetic model parameters of MA2 for Pb (II) and Cu (II) adsorption in single heavy metal ion system.

Models	Parameters	Values							
		Pb (II)				Cu (II)			
		50 mg/L	100 mg/L	150 mg/L	200 mg/L	50 mg/L	100 mg/L	150 mg/L	200 mg/L
Pseudo-first-order	k_1 (min^{-1})	0.0243	0.0125	0.0122	0.0119	0.1493	0.0662	0.0862	0.0586
	q_e (mg/g)	37.23	80.33	106.12	131.05	46.34	79.96	100.86	120.91
	R^2	0.8257	0.9653	0.9635	0.9670	0.9977	0.9278	0.9130	0.8856
Pseudo-second-order	k_2 (g/(mg·min)	0.0008	0.0002	0.0001	0.0001	0.0075	0.0011	0.0011	0.0006
	q_e (mg/g)	41.57	91.65	122.18	151.68	47.71	87.22	109.04	133.29
	R^2	0.9127	0.9799	0.9896	0.9934	0.9979	0.9778	0.9649	0.9545
Intraparticle diffusion	k_{p1} (mg/(g·$min^{1/2}$)	3.1126	5.3085	7.2201	8.8114	10.4754	13.0413	18.4766	21.0901
	C (mg/g)	0.7775	0.7610	0.2434	0.0280	0.3237	0.1399	0.2167	0.3231
	R^2	0.9402	0.9869	0.9991	0.9998	0.9771	0.9948	0.9849	0.9739
	k_{p2} (mg/(g·$min^{1/2}$)	1.0684	0.8095	1.8624	1.9616	0.1513	2.0895	2.7819	3.7278
	C (mg/g)	17.6181	63.0045	65.7967	87.3936	44.6244	54.1752	66.9122	72.4093
	R^2	0.8512	0.6288	0.7201	0.8101	0.3683	0.8665	0.9226	0.9437
Elovich	α (mg/(mg·min)	6.3605	3.4909	3.9524	4.5528	2690150	64.86	179.29	59.96
	β (mg/g)	0.1516	0.0554	0.0399	0.0317	0.4061	0.0829	0.0737	0.0502
	R^2	0.9735	0.9740	0.9708	0.9776	0.9859	0.9952	0.9935	0.9933

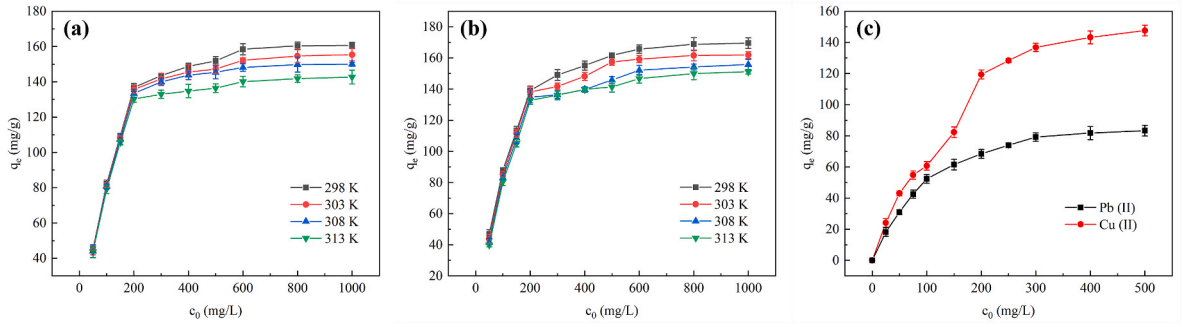

Fig. 9. Adsorption isotherm for the adsorption of Pb (II) (a) and Cu (II) (b) in single heavy metal ion system and Pb (II) and Cu (II) (c) in binary heavy metal ion system.

Table 3
Isotherm model parameters of MA2 for Pb (II) and Cu (II) adsorption in single heavy metal ion system.

Models	Parameters	Values							
		Pb (II)				Cu (II)			
		298 K	303 K	308 K	313 K	298 K	303 K	308 K	313 K
Langmuir	K_L (L/mg)	0.0631	0.0646	0.0630	0.0659	0.0863	0.0663	0.0574	0.0502
	q_m (mg/g)	161.53	156.77	153.52	145.02	166.39	162.74	156.26	153.97
	R^2	0.9841	0.9864	0.9888	0.9829	0.9725	0.9842	0.9710	0.9676
Freundlich	K_F (mg/g)/(mg/L)^n)	54.88	54.95	54.46	53.56	60.02	55.72	52.15	49.99
	n	0.1724	0.1669	0.1643	0.1578	0.1663	0.1714	0.1737	0.1763
	R^2	0.8623	0.8371	0.8161	0.7988	0.8998	0.8449	0.8159	0.7904
Temkin	K_T (L/g)	2.7658	3.0323	3.0456	3.7101	4.4465	2.7019	2.2003	1.7909
	B_T	22.28	21.34	20.83	19.15	21.94	22.59	22.11	22.24
	R^2	0.9316	0.9098	0.8925	0.8736	0.9613	0.9135	0.8834	0.8626
Dubinin-Radushkevich	K_{DR} (mol^2/kJ^2)	7.98	9.53	11.31	10.53	3.56	13.28	20.44	27.53
	q_{DR} (mg/g)	143.08	140.21	137.88	130.96	149.19	148.13	142.73	140.29
	E (kJ/mol)	0.2503	0.2291	0.2103	0.2179	0.3748	0.1940	0.1564	0.1348
	R^2	0.6723	0.7461	0.7712	0.7833	0.6997	0.8426	0.8946	0.9142

Besides, MA2 displays excellent adsorption properties compared to other types of aerogels, which are prepared by freeze-drying or under subcritical conditions. Gratifyingly, MA2 can gain high adsorption capacity by a simple atmospheric pressure drying environment. This may be related to the three-dimensional mesh-like structure, the large specific surface area and the abundance of sulfhydryl functional groups on the surface of the MA2 aerogel. This reveals that MA2 is an excellent adsorbent for the removal of heavy metal ions from wastewater.

3.2.5. Adsorption thermodynamics

Temperature has an impact on the adsorption of Pb (II) and Cu (II) on MA2 as shown by Fig. 10a. The adsorption capacity of Pb (II) and Cu (II) on MA2 is significantly reduced when the temperature increases. According to plot *lnkc* versus *1/T* provides the thermodynamic parameters related to the adsorption process, including entropy change (ΔS^0) and enthalpy change (ΔH^0) (Fig. 10b) (Chakraborty et al., 2021). The calculation results are listed in Table 5.

ΔG^0 was found to be negative for all different temperatures, and the negative values of ΔG^0 tends to increase at higher temperatures, implying that the adsorption is spontaneous and feasible for Pb (II) and Cu (II) on MA2, and a higher temperature will lead to a lower adsorption capacity. The negative values of ΔH^0 implies that the adsorption process

Table 4
Comparison of the adsorption performance of MA2 with different adsorbents for removing Pb (II) and Cu (II) from aqueous solutions.

Adsorbents	Adsorbate	q_m (mg/g)	Conditions	Reference
Geopolymer gel (NaSi-MGP)	Pb^{2+}	137.7	c_0- 20–140 mg/L; pH-6; T-303 K; dose- 30 mg; time- 250 min	Wang et al. (2021)
	Cu^{2+}	90		
Cellulose nanofiber/chitosan/montmorillonite aerogel (CNF/CS/MMT)	Pb^{2+}	170.19	c_0- 0–500 mg/L; pH-2; T-298 K; dose- 100 mg; time- 60 min	Rong et al. (2021)
	Cu^{2+}	181.93		
Hydroxypropyl-cyclodextrin-graphene/Fe_3O_4 nanomaterial (HP-β-CD-GO/Fe_3O_4)	Pb^{2+}	50.39	c_0- 1000 mg/L; pH-5; T-303 K; dose- 100 mg; time- 15 min	Tahir et al. (2019)
	Cu^{2+}	17.91	c_0- 1000 mg/L; pH-6; T-313 K; dose- 100 mg; time- 15 min	
Amino-modified silica aerogel	Cu^{2+}	47.6	c_0- 50–500 mg/L; pH-6; T-298 K; dose- 500 mg; time- 24 h	Faghihian et al. (2014)
Amino-functionalized bovine serum albumin amyloid fibrils aerogel (BFP25)	Cu^{2+}	82.8	c_0- 25–250 mg/L; pH-5; T-303 K; dose- 25 mg; time- 540 min	Wei et al. (2022)
Nanocellulose/sodium alginate/carboxymethyl-chitosan aerogel (NSC)	Pb^{2+}	472.59	c_0- 50–300 mg/L; pH-5; T-303 K; dose- 30 mg; time- 180 min	Li et al. (2021)
	Cu^{2+}	169.94		
Poplar saw dust (PSD) derived biochar (PB-700 °C)	Pb^{2+}	62.68	c_0- 200–400 mg/L; pH-5; T-298 K; dose-100 mg; time-600 min	Cheng et al. (2021)
Amino-modified Resorcinol-formaldehyde aerogel (RF-A10%)	Pb^{2+}	156.25	c_0- 20–500 mg/L; pH-6; T- 298 K; dose- 1 g/L; time- 12 h	Motahari et al. (2016)
Graphene oxide/carboxymethyl chitosan aerogel (GO/CMC-5)	Pb^{2+}	249.38	c_0- 25–600 mg/L; pH-5; T- 303 K; time- 720 min	Luo et al. (2019)
	Cu^{2+}	95.37		
Sulfhydryl modified chitosan aerogel (SMCA)	Pb^{2+}	38.87	c_0- 200 mg/L; pH-5; T- 298 K; dose-200 mg; time- 12 h	Zhang et al. (2020)
	Cu^{2+}	81.15	c_0- 200 mg/L; pH-6; T- 298 K; dose-200 mg; time- 10 h	
Mercapto-functionalized aerogel (MA2)	Pb^{2+}	161.53	c_0- 50–1000 mg/L; pH-5; T-298 K; dose-1 g/L; time- 360 min	This work
	Cu^{2+}	166.39	c_0- 50–1000 mg/L; pH-5; T-298 K; dose-1 g/L; time- 180 min	

is exothermic and the negative values of ΔS^0 demonstrates that the randomness decreasing at solid-liquid interface. Similar thermodynamic behavior has been found in related literature for the adsorption of Pb (II) ion on phenylthiosemicarbazide-functionalized UiO-66-NH_2 (Tang et al., 2021).

3.3. Selective adsorption of Pb (II) and Cu (II)

A study was investigated for the selective adsorption of MA2 towards Pb (II) and Cu (II) involving binary heavy metal ions at different times and various initial concentrations. Fig. 8c demonstrates that the adsorption equilibrium was reached around 120 min for Cu (II), while adsorption equilibrium was reached around 720 min for Pb (II), indicating that Cu (II) adsorption was much faster than Pb (II). Moreover, the maximum equilibrium adsorption capacity of MA2 for the adsorption of Cu (II) is much greater compared with Pb (II), suggesting that Cu (II) is more readily adsorbed onto MA2. (Fig. 9c). From Tables S2–S3, it is observed that the pseudo second order kinetic equations can better fit the adsorption process in the binary metal ion system, the adsorption of Pb (II) and Cu (II) also corresponds well to the Langmuir isotherm model at 298 K (Fig. S6 and Fig. S7). Selective adsorption experiments showed that MA2 reached adsorption equilibrium faster for Cu (II) than for Pb (II) and had a higher adsorption capacity than Pb (II), indicating that MA2 could preferentially adsorb Cu (II).

The separation coefficient (K_d) and the selectivity coefficient (α) are calculated in Table 6 (Xu et al., 2021; Ji et al., 2022). It can be seen that at pH < 4, MA2 shows higher selectivity for Cu (II) with increasing of pH. At 4 < pH < 6, the selectivity of MA2 for Cu (II) reduces with an increasing pH, but still remains selective for Cu (II). Coupled with the adsorption experiment data, and further supported by DFT calculations, it is demonstrated that the mercaptan group has a higher affinity for binding Cu (II) than Pb (II).

3.4. Recycling performance and practical application

The reusability of adsorbents was evaluated using 10 mg of MA2 after Pb (II) and Cu (II) adsorption and 25 mL 0.1 M HCl solution, and the experimental results were displayed in Fig. 11. The removal efficiency of MA2 was 90.12% and 92.54% for the first replicate experiment for Pb (II) and Cu (II) and still remained at 83.86% and 65.28% after 5 consecutive adsorption-desorption cycles experiments, respectively. As the acidic conditions do not destroy the sulfhydryl functional groups, this is probably attributed to the fact that the heavy metal ions were not completely eluted during the elution process, resulting in a decrease in adsorption efficiency (Fang et al., 2005; Ji et al., 2019). Studies have demonstrated that the acid solution can effectively elute the Cu (II) ions from the adsorbent (Awual et al., 2013). After five recycling times, the removal efficiency of Cu (II) decreased significantly, indicating that Cu (II) were more difficult to be eluted from MA2, probably owing to the stronger bonding of Cu (II) ions to the adsorbent, which is further supported by the DFT results.

One practical wastewater specimen was obtained from a chemical plant in Xi'an, Shaanxi Province. The suspension was removed from wastewater samples by filtration using a 0.22 μm diameter microporous membrane. Adsorption experiments were carried out by immersing 100 mg of MA2 into 100 mL of wastewater at pH 5 and the adsorption was continued for 12 h. The residual concentration of Pb (II) and Cu (II) ions in the wastewater was tested. It can be seen from Fig. S8 that 73 mg/L of Pb (II) and 58 mg/L of Cu (II) were detected in the practical wastewater, both of which are extremely high levels and significantly higher than the USEPA and WHO drinking water standards. The treatment of this wastewater using MA2 adsorbent resulted in a removal of 74.2% for Pb (II) and 82.6% for Cu (II) and the pH changed from 5 to 7.13. This result indicates that the MA2 adsorbent was effective in removing Pb (II) and Cu (II) from the wastewater.

3.5. Adsorption mechanism

3.5.1. XPS analysis

For an in-depth explanation of the adsorption mechanism, the XPS of MA2 before and after Pb (II) and Cu (II) adsorption were evaluated. Fig. 12a shows the full spectrum before and after adsorption of the

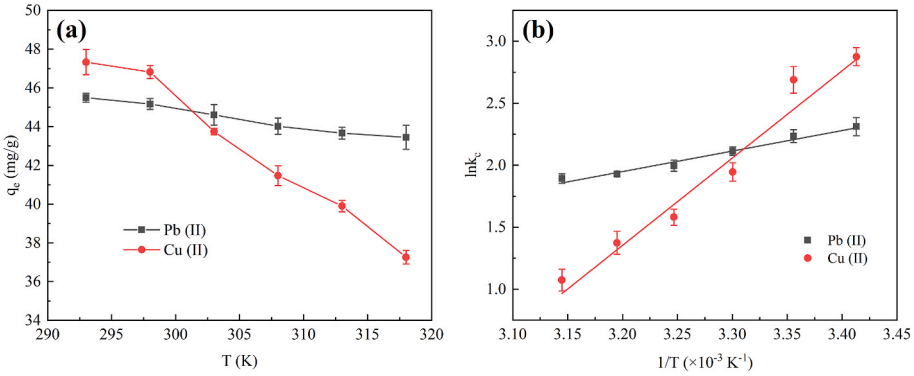

Fig. 10. Effect of temperature (a) and thermodynamic curves (b) on the adsorption of Pb (II) and Cu (II) by MA2.

Table 5
Thermodynamic parameters of MA2 for Pb (II) and Cu (II) adsorption.

T/K	Pb (II)			Cu (II)		
	△G^0/(kJ/mol)	△H^0/(kJ/mol)	△S^0/(J/(mol·K)	△G^0/(kJ/mol)	△H^0/(kJ/mol)	△S^0/(J/(mol·K)
293	−5.624	−13.893	−28.222	−7.058	−59.099	−177.614
298	−5.483			−6.171		
303	−5.341			−5.282		
308	−5.201			−4.394		
313	−5.059			−3.506		
318	−4.918			−2.618		

Table 6
Selective adsorption parameters of MA2 for Pb (II) and Cu (II) adsorption.

pH	K_d (Pb (II))(L/g)	K_d (Cu (II))(L/g)	α
1	0.09	0.40	4.48
2	0.11	0.67	6.33
3	0.21	1.66	7.99
4	0.53	4.38	8.20
5	1.63	6.19	3.79
6	1.83	6.81	3.73

adsorbent. MA2 was primarily made up of four elements comprising C, O, Si and S, and the presence of S is indicative of the successful synthesis of the adsorbent. After adsorption, a characteristic peak of Pb 4f was observed in MA2-Pb, and a Cu 2p peak also appeared in MA2-Cu.

From Fig. 12b, the spectrum of Pb 4f showed a binding energy of 138.15 eV for Pb 4f7/2 and 143.08 eV for Pb 4f5/2, which corresponded to Pb (II) and indicated that Pb (II) was successfully adsorbed. (Chen et al., 2020; Hou et al., 2021). From Fig. 12c, the peak of Cu 2p can be split into Cu 2p1/2 (954.34 eV) and Cu 2p3/2 (934.78 eV), indicating that Cu (II) was successfully adsorbed on MA2 (Sardarian et al., 2021). Thus, there is a critical role for chelation between MA2 and metal ions in the adsorption process.

The C1s spectrum of MA2 (Fig. 12d) can be split into three peaks at 284.80, 283.38 and 285.88eV, corresponding to the C–C, C–Si and C–S bonds, respectively. However, compared with that of MA2, the binding energy of C–S in MA2-Pb (Fig. 12e) displayed a slight shift (~ 0.5 eV), and a slight shift of the C–S binding energy (~0.2 eV) was also observed in MA2-Cu (Fig. 12f), indicating that the –SH functional group was engaged for Pb (II) and Cu (II) adsorption.

High resolution S 2p spectra are exhibited in Fig. 12g-**12i**. The peaks at the 163.51 and 164.92 eV are allocated to S 2p3/2 and S 2p1/2, which belong to sulfhydryl group (Heidari et al., 2018; Liang et al., 2022). After adsorption of Pb (II), they both shifted to 164.31 and 165.74 eV, respectively. While after adsorption of Cu (II), the S 2p3/2 shifted to 164.25 eV, and S 2p1/2 moved to 165.52 eV, presumably attributed to

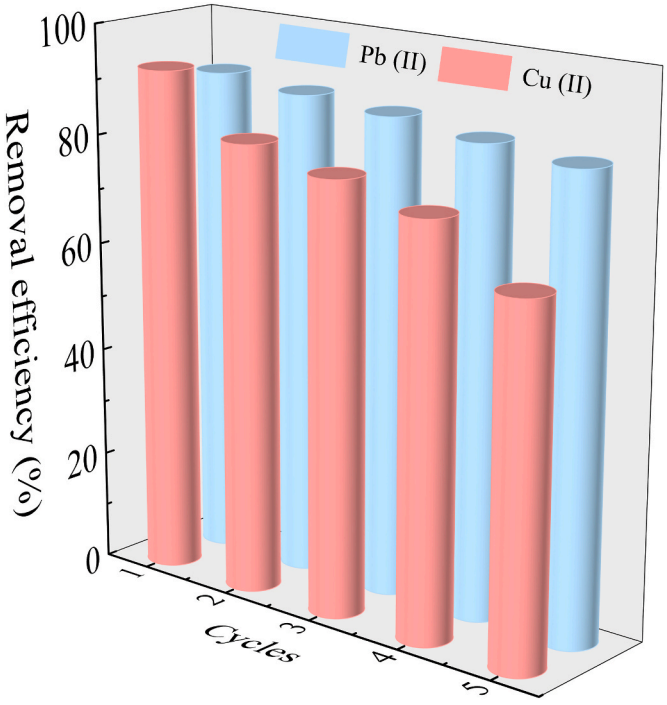

Fig. 11. Regeneration experiments for the removal of Pb (II) and Cu (II) by MA2.

the electron-donating interactions of the S atom of the –SH groups to Pb (II) and Cu (II) (Geng et al., 2017; Tang et al., 2021). The XPS results showed that the –SH functional groups of MA2 were able to chelate Pb (II) and Cu (II) during the adsorption process.

3.5.2. DFT calculation

The optimized molecular model for MA2 binding of Pb (II) and Cu (II) was shown in Fig. S9. Fig. 13 showed the adsorption energy (E_{ads}) of the adsorbent with associated ions for the adsorption and regeneration process. The negative E_{ads} denotes favorable adsorption, whereas a positive E_{ads} represents an energetically unfavorable process (Wang et al., 2020). The adsorption energies calculated by DFT showed that there was lower E_{ads} for Cu (−2.72 eV) adsorbed on MA2 than for Pb (−0.80 eV), demonstrating that Cu (II) is likely to be more stable than Pb (II) adsorbed on MA2. On the other hand, it was also shown that Cu (II) was more readily adsorbed on MA2 in adsorption experiments with single and binary metal ions systems. Notably, the equilibrium adsorption capacity of Cu (II) was apparently greater than Pb (II) in the binary metal ions system, which also indicated that Cu (II) ions was prefavourably trapped onto MA2. To understand the ease of regeneration in

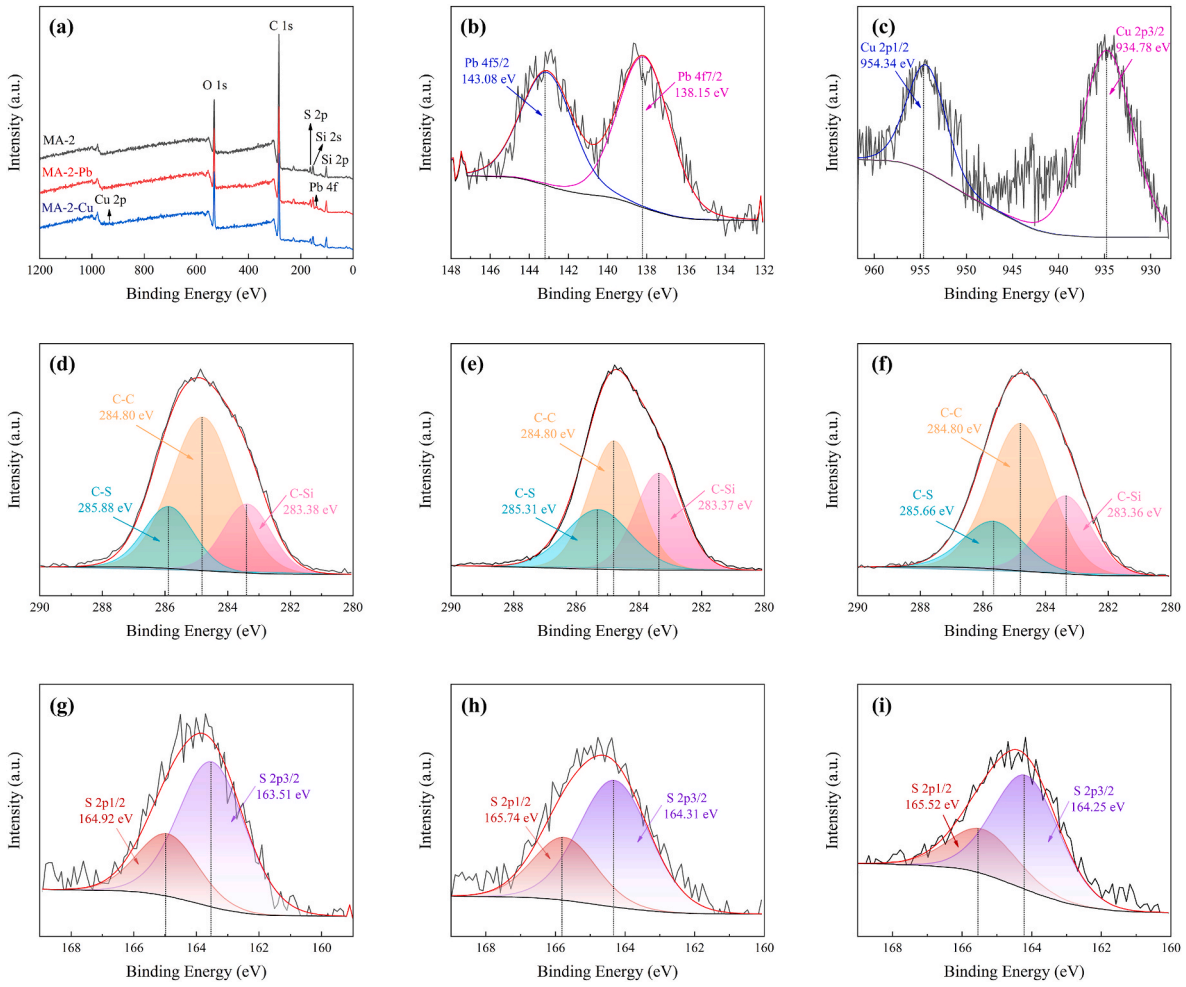

Fig. 12. XPS spectra of mercapto-functionalized aerogel before and after Pb (II) and Cu (II) adsorption. (a) full spectrum of MA2, MA2-Pb and MA2-Cu, (b) Pb 4f high-resolution spectra of MA2-Pb, (c) Cu 2p high-resolution spectra of MA2-Cu, (d) C1s XPS spectra of MA2, MA2-Pb (e) and MA2-Cu (f), S 2p XPS spectra of MA2 (g), MA2-Pb (h) and MA2-Cu (i).

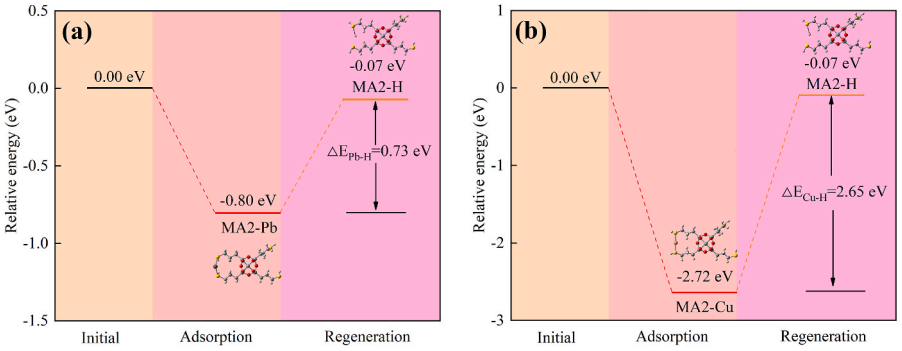

Fig. 13. The optimized adsorption profiles and the energy changes during adsorption and regeneration. (a) MA2-Pb, (b) MA2-Cu.

terms of energy change, we evaluated the embodied energy that was needed to regenerate adsorbents trapped with Pb (II) and Cu (II) by H^+, named $\Delta E_{Pb\text{-}H}$ and $\Delta E_{Cu\text{-}H}$, respectively (Fig. 13). $\Delta E_{Pb\text{-}H}$ and $\Delta E_{Cu\text{-}H}$ for MA2 were 0.72 and 2.64 eV, respectively. Compared to $\Delta E_{Cu\text{-}H}$, the results revealed that MA2-Pb takes only less of energy for regeneration, which is consistent with the results obtained from recycling experiments.

Fig. 14 indicated the variations of HOMO and LUMO before and after adsorption, as well as its gap energy (E_{gap}). For MA2, the LUMO is primarily distributed along the Si–O–Si backbone, and HOMO is partly found along the –SH group. After the adsorption of Pb (II) and Cu (II), both LUMO and HOMO changed markedly, which indicates that these metals were succeeding in binding to MA2. In addition, as the calculated E_{gap} of the Cu complex was larger than that of the Pb complex, showing that the Cu complex has a higher molecular stability, which followed the positive correlation between the stability of the metal complex and the E_{gap} (Wang et al., 2019). When the Cu (II) ion was preferentially trapped by the MA2 molecule, it is difficult to disrupt the coordination bond that

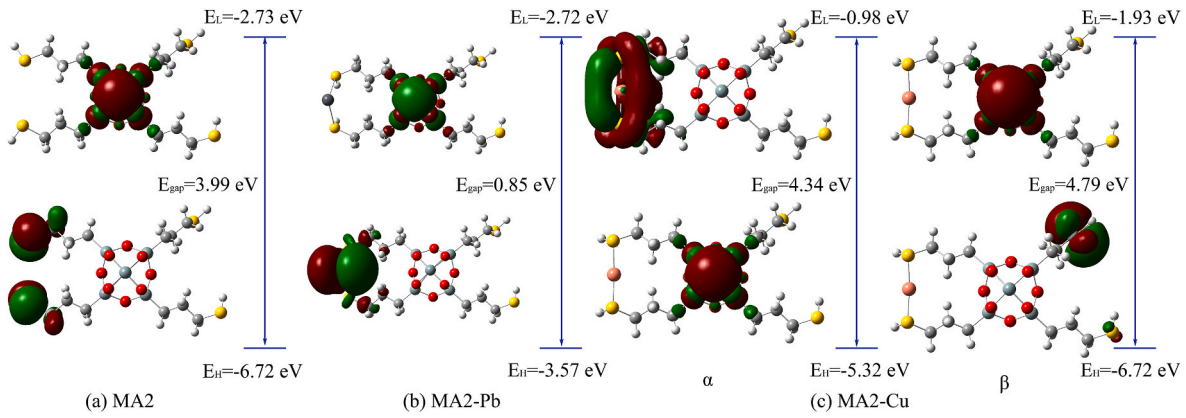

Fig. 14. HOMO and LUMO plots of MA2 (a), MA2-Pb (b) and MA2-Cu (c).

exists between the Cu (II) ion and the –SH functional group, making it much harder for Pb (II) to exchange with Cu (II). This result has been validated by adsorption experiments and confirmed by previous literature (Wang et al., 2021).

3.6. LCA analysis

3.6.1. Environmental impacts of MA2

The environmental impact of producing 1 kg of MA2 is shown **in** Table 7. The highest impact value is achieved in PED *i.e.* 2630 MJ. At the same time the production process also produced more greenhouse gases, leading to an increase in the greenhouse effect. In addition to the two above, the maximum value produced during MA2 manufacture is only 0.466 in acidification potential, so the MA2 manufacturing process mainly affects GWP and PED.

In order to find a way to be able to further analyze the environmental impact of MA2 in production, the contribution of each component to the environmental impact was analyzed. Fig. 15 shows the environmental impacts of producing 1 kg of MA2. In order to further analyze the environmental impact produced by the sorbent during production, the environmental impact categories from all raw materials were normalized to be 100% of all factors for each impact category. All materials required for production are dominated by ethanol and n-hexane. There are 81.82%, 68.64%, 55.29%, 40.53%, 45.43%, 54.50%, and 65.51% contributions by ethanol to GWP, AP, ADP, EP, ODP, FOFP, and PED, respectively, and 10.52%, 21.09%, 39.41%, 32.07%, 47.51%, 39.95%, and 27.83% contributions by n-hexane. In addition, Table 1 shows that the amount of TEOS used is only 0.94 kg, which is approximately 2.5% of the amount of n-hexane used, but contributes 4.3% to the GWP of the MA2 synthesizing phase. In order to explore a less environmentally impactful way of synthesizing MA2, the three raw materials above had to be replaced or recycled. It is possible to collect the evaporated ethanol and n-hexane from the MA2 production method as they have volatile that are heated during its production. The recycling of ethanol and n-hexane will significantly alter the environmental impact of MA2 and thus reduce it. It is worth investigating the alternative silica sources, like sodium silicate (i.e., water glass), which has a lower environmental impact than TEOS (Guo et al., 2015).

Table 7
The environmental impact of the production of 1 kg of MA2.

Category	Unit	Result
GWP	kg CO_2 eq	118
AP	kg SO_2 eq	0.466
ADP	kg antimony eq	0.018
EP	kg PO_4^{3-} eq	0.064
ODP	kg CFC^{-11} eq	1.9E-05
POFP	kg NMVOC eq	0.405
PED	MJ	2630

3.6.2. Impact score and uncertainty analysis

The environmental externalities of MA2 can be better understood by assessing sensitivity using LCI values. The uncertainty analysis takes into account any uncertainty associated with the computation of the influence fraction owing to possible deviations in the use of raw materials and energy in the manufacture of MA2. The uncertainties and the maximum and minimum values of the results at 95% confidence intervals for each environmental impact category are given in Table 8. As the production of the MA2 was carried out at laboratory scale, some variation in the simulated environmental effects may be expected in large volume industrial scale production. Therefore, uncertainty analyses presenting maximum and minimum impact values were presented to provide a clearer perspective on the process dynamics and environmental footprint of different production scales.

4. Conclusions

In summary, mercapto-functionalized aerogels were fabricated to eliminate Pb (II) and Cu (II) from solutions. Various characterizations and experiments showed that MA2 exhibited the most effective adsorption property with the maximum adsorption amounts of 163.99 mg/g and 172.41 mg/g for Pb (II) and Cu (II) in the single ion system, respectively, and 90.42 mg/g and 161.29 mg/g for Pb (II) and Cu (II) in the binary ion system, respectively. Adsorption kinetics corresponded to a pseudo-second-order model, and adsorption isotherms were consistent with the Langmuir model, suggesting that Pb (II) and Cu (II) were adsorbed in a monolayer onto adsorbent surfaces and chemisorption was the rate-controlling step. Selective adsorption experiments revealed that the equilibrium adsorption capacity for Cu (II) was remarkably greater than for Pb (II) and selectivity factor α showed a greater selectivity for Cu (II), indicating that Cu (II) was more easily adsorbed on MA2. XPS and DFT results implied that the electron transfer between MA2 and the heavy metal ions occurred and the main adsorption mechanism of MA2 was coordination chelation through the –SH groups with Pb (II) and Cu (II). The DFT calculations also revealed that Cu (II) has a lower E_{ads} and a higher E_{gap} than Pb (II), indicating that Cu (II) was more stable for adsorption on MA2 and more difficult to exchange by Pb (II). In the end, the environmental impact of producing 1 kg of MA2 was investigated. By analyzing the production process of MA2, environmental hotspots were identified and solutions proposed.

Compliance with ethical standards

The authors declare no conflict of interest. This article does not contain any studies with human participants or animals. Informed consent was obtained from all individual participants included in the

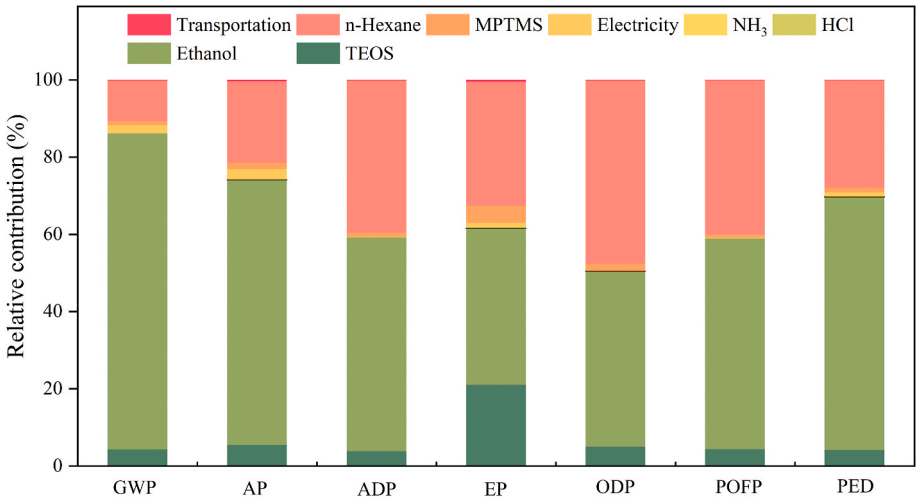

Fig. 15. Relative contribution of environmental impact indicators for MA2.

Table 8
Environmental impact data quality assessment results.

Category	Result	Uncertainty	Upper and lower limits of result
GWP(kg CO_2 eq)	118	12.78%	[103, 133]
AP(kg SO_2 eq)	0.466	11.12%	[0.414, 0.518]
ADP(kg antimony eq.)	0.0179	15.31%	[0.0151, 0.0206]
EP(kg PO_4^{3-}eq)	0.0636	8.12%	[0.0585, 0.0688]
ODP(kg CFC^{-11} eq)	1.9E-05	16.30%	[1.59E-05,2.21E-05]
POFP(kg NMVOC eq)	0.405	9.38%	[0.367,0.443]
PED(MJ)	2630	12.87%	[2290, 2970]

study.

CRediT authorship contribution statement

Yaoyao Zhang: Investigation, Conceptualization, Methodology, Validation, Data curation, Formal analysis, Writing – original draft. **Kangze Yuan:** Data curation, Formal analysis, Writing – original draft, Writing – review & editing. **Luca Magagnin:** Supervision, Writing – review & editing. **Xishe Wu:** Validation. **Zhenyi Jiang:** Formal analysis. **Wei Wang:** Methodology, Funding acquisition, Supervision, Writing – review & editing.

Declaration of competing interest

The authors declare that they have no known competing financial interests or personal relationships that could have appeared to influence the work reported in this paper.

Data availability

Data will be made available on request.

Acknowledgments

This work was supported by the National Natural Science Foundation of China (51678059), the Key Research and Development Program of Shaanxi Province (2019GY-179), the Innovative Research Team for Science and Technology of Shaanxi Province (2022TD-04), the National Foreign Expert Project of China (G2021171031L).

Appendix A. Supplementary data

Supplementary data to this article can be found online at https://doi.org/10.1016/j.jclepro.2023.136126.

References

Abdel-Magied, A.F., Abdelhamid, H.N., Ashour, R.M., Fu, L., Dowaidar, M., Xia, W., Forsberg, K., 2022. Magnetic metal-organic frameworks for efficient removal of cadmium(II), and lead(II) from aqueous solution. J. Environ. Chem. Eng. 10 (3), 107467 https://doi.org/10.1016/j.jece.2022.107467.

Alqadami, A.A., Naushad, Mu, Alothman, Z.A., Alsuhybani, M., Algamdi, M., 2020. Excellent adsorptive performance of a new nanocomposite for removal of toxic Pb(II) from aqueous environment: adsorption mechanism and modeling analysis. J. Hazard Mater. 389, 121896 https://doi.org/10.1016/j.jhazmat.2019.121896.

Awual, M.R., 2019a. An efficient composite material for selective lead(II) monitoring and removal from wastewater. J. Environ. Chem. Eng. 7 (3), 103087 https://doi.org/10.1016/j.jece.2019.103087.

Awual, M.R., 2019b. Novel conjugated hybrid material for efficient lead(II) capturing from contaminated wastewater. Mater. Sci. Eng. C. 101, 686–695. https://doi.org/10.1016/j.msec.2019.04.015.

Awual, M.R., Ismael, M., Yaita, T., El-Safty, S.A., Shiwaku, H., Okamoto, Y., Suzuki, S., 2013. Trace copper(II) ions detection and removal from water using novel ligand modified composite adsorbent. Chem. Eng. J. 222, 67–76. https://doi.org/10.1016/j.cej.2013.02.042.

Betiha, M.A., Moustafa, Y.M., El-Shahat, M.F., Rafik, E., 2020. Polyvinylpyrrolidone-Aminopropyl-SBA-15 schiff Base hybrid for efficient removal of divalent heavy metal cations from wastewater. J. Hazard Mater. 397, 122675 https://doi.org/10.1016/j.jhazmat.2020.122675.

Blanchard, G., Maunaye, M., Martin, G., 1984. Removal of heavy metals from waters by means of natural zeolites. Water Res. 18 (12), 1501–1507. https://doi.org/10.1016/0043-1354(84)90124-6.

Cao, B., Qu, J., Yuan, Y., Zhang, W., Miao, X., Zhang, X., Xu, Y., Han, T., Song, H., Ma, S., Tian, X., Zhang, Y., 2022. Efficient scavenging of aqueous Pb(II)/Cd(II) by sulfide-iron decorated biochar: performance, mechanisms and reusability exploration. J. Environ. Chem. Eng. 10 (3), 107531 https://doi.org/10.1016/j.jece.2022.107531.

Chakraborty, R., Verma, R., Asthana, A., Vidya, S.S., Singh, A.K., 2021. Adsorption of hazardous chromium (VI) ions from aqueous solutions using modified sawdust: kinetics, isotherm and thermodynamic modelling. Int. J. Anal. Chem. 101, 911–928. https://doi.org/10.1080/03067319.2019.1673743.

Chen, K., Feng, Q., Feng, Y., Ma, D., Wang, D., Liu, Z., Zhu, W., Li, X., Qin, F., Feng, J., 2022. Ultrafast removal of humic acid by amine-modified silica aerogel: insights from experiments and density functional theory calculation. Chem. Eng. J. 435, 135171 https://doi.org/10.1016/j.cej.2022.135171.

Chen, K., Feng, Q., Ma, D., Huang, X., 2021. Hydroxyl modification of silica aerogel: an effective adsorbent for cationic and anionic dyes. Colloid Surf. A Physicochem. Eng. Asp. 616, 126331 https://doi.org/10.1016/j.colsurfa.2021.126331.

Chen, W., Lu, Z., Xiao, B., Gu, P., Yao, W., Xing, J., Asiri, A.M., Alamry, K.A., Wang, X., Wang, S., 2019. Enhanced removal of lead ions from aqueous solution by iron oxide nanomaterials with cobalt and nickel doping. J. Clean. Prod. 211, 1250–1258. https://doi.org/10.1016/j.jclepro.2018.11.254.

Chen, Y., Yang, Z., Zhang, Q., Fu, D., Chen, P., Li, R., Liu, H., Wang, Y., Liu, Y., Lv, W., Liu, G., 2020. Effect of tartaric acid on the adsorption of Pb (II) via humin: kinetics and mechanism. J. Taiwan Inst. Chem. Eng. 107, 79–88. https://doi.org/10.1016/j.jtice.2019.11.012.

Cheng, S., Liu, Y., Xing, B., Qin, X., Zhang, C., Xia, H., 2021. Lead and cadmium clean removal from wastewater by sustainable biochar derived from poplar saw dust. J. Clean. Prod. 314, 128074 https://doi.org/10.1016/j.jclepro.2021.128074.
Dubinin, M.M., 1947. The equation of the characteristic curve of activated charcoal. Phys. Chem. Sect. 327–329.
Ecer, Ü., Yılmaz, Ş., Şahan, T., 2018. Highly efficient Cd(II) adsorption using mercapto-modified bentonite as a novel adsorbent: an experimental design application based on response surface methodology for optimization. Water Sci. Technol. 78 (6), 1348–1360. https://doi.org/10.2166/wst.2018.400.
Ehgartner, C.R., Werner, V., Selz, S., Hüsing, N., Feinle, A., 2021. Carboxylic acid-modified polysilsesquioxane aerogels for the selective and reversible complexation of heavy metals and organic molecules. Microporous Mesoporous Mater. 312, 110759 https://doi.org/10.1016/j.micromeso.2020.110759.
European Commission, 2010. ILCD Handbook - Framework and Requirements for Life Cycle Impact Assessment Models and Indicators, first ed. March 2010. Luxembourg.
Faghihian, H., Nourmoradi, H., Shokouhi, M., 2014. Removal of copper (II) and nickel (II) from aqueous media using silica aerogel modified with amino propyl triethoxysilane as an adsorbent: equilibrium, kinetic, and isotherms study. Desalination Water Treat. 52 (1–3), 305–313. https://doi.org/10.1080/19443994.2013.785367.
Fan, J., Cai, C., Chi, H., Reid, B.J., Coulon, F., Zhang, Y., Hou, Y., 2020. Remediation of cadmium and lead polluted soil using thiol-modified biochar. J. Hazard Mater. 388, 122037 https://doi.org/10.1016/j.jhazmat.2020.122037.
Fang, G., Tan, J., Yan, X., 2005. An ion-imprinted functionalized silica gel sorbent prepared by a surface imprinting technique combined with a sol-gel process for selective solid-phase extraction of cadmium(II). Anal. Chem. 77 (6), 1734–1739. https://doi.org/10.1021/ac048570v.
Ferrão, P.C., 2009. Industrial Ecology-Principles and Tools (In Portuguese).
Franco, P., Cardea, S., Tabernero, A., De Marco, I., 2021. Porous aerogels and adsorption of pollutants from water and air: a review. Molecules 26 (15), 4440. https://doi.org/10.3390/molecules26154440.
Freundlich, H.M.F.U., 1906. Uber die adsorption in losungen. Zeitschrift fur Physikalische Chemie-Leipzig, pp. 385–470.
Frisch, M.E., Trucks, G.W., Schlegel, H.B., Scuseria, G.E., Robb, M.A., Cheeseman, J.R., Fox, D.J., 2009. Gaussian, Inc (Wallingford CT. Wallingford CT).
Ganesamoorthy, R., Vadivel, V.K., Kumar, R., Kushwaha, O.S., Mamane, H., 2021. Aerogels for water treatment: a review. J. Clean. Prod. 329, 129713 https://doi.org/10.1016/j.jclepro.2021.129713.
Geng, B., Wang, H., Wu, S., Ru, J., Tong, C., Chen, Y., Liu, H., Wu, S., Liu, X., 2017. Surface-tailored nanocellulose aerogels with thiol-functional moieties for highly efficient and selective removal of Hg(II) ions from water. ACS Sustain. Chem. Eng. 5, 11715–11726. https://doi.org/10.1021/acssuschemeng.7b03188.
Ghaedi, A.M., Panahimehr, M., Nejad, A.R.S., Hosseini, S.J., Vafaei, A., Baneshi, M.M., 2018. Factorial experimental design for the optimization of highly selective adsorption removal of lead and copper ions using metal organic framework MOF-2 (Cd). J. Mol. Liq. 272, 15–26. https://doi.org/10.1016/j.molliq.2018.09.051.
Guo, Y., Wang, H., Zeng, L., 2015. SiO_2 aerogels prepared by ambient pressure drying with ternary azeotropes as components of pore fluid. J. Non-Cryst. Solids 428, 1–5. https://doi.org/10.1016/j.jnoncrysol.2015.07.030.
Gupta, V.K., Suhas, 2009. Application of low-cost adsorbents for dye removal – a review. J. Environ. Manag. 90 (8), 2313–2342. https://doi.org/10.1016/j.jenvman.2008.11.017.
Han, J., Liang, X., Xu, Y., Xu, Y., 2015. Removal of Cu^{2+} from aqueous solution by adsorption onto mercapto functionalized palygorskite. J. Ind. Eng. Chem. 23, 307–315. https://doi.org/10.1016/j.jiec.2014.08.034.
Heidari, B.S., Cheraghchi, V.-S., Motahari, S., Motlagh, G.H., Davachi, S.M., 2018. Optimized mercapto-modified resorcinol formaldehyde xerogel for adsorption of lead and copper ions from aqueous solutions. J. Sol. Gel Sci. Technol. 88, 236–248. https://doi.org/10.1007/s10971-018-4782-z.
Hossaini-Zahed, S.-S., Khanlari, S., Bakhtiari, O., Tofighy, M.A., Hadadpour, S., Rajabzadeh, S., Zhang, P., Matsuyama, H., Mohammadi, T., 2022. Evaluation of process condition impact on copper and lead ions removal from water using goethite incorporated nanocomposite ultrafiltration adsorptive membranes. Water Sci. Technol. 85 (4), 1053–1064. https://doi.org/10.2166/wst.2022.024.
Hou, L., Qin, G., Qu, Y., Yang, C., Rao, X., Gao, Y., Zhu, X., 2021. Fabrication of recoverable magnetic composite material based on graphene oxide for fast removal of lead and cadmium ions from aqueous solution. J. Chem. Technol. Biotechnol. 96 (5), 1345–1357. https://doi.org/10.1002/jctb.6655.
Hüsing, N., Schubert, U., 1997. Organofunctional silica aerogels. J. Sol. Gel Sci. Technol. 8, 807–812. https://doi.org/10.1007/BF02436942.
Ibrahim, N.A., Abdellatif, F.H.H., Hasanin, M.S., Abdellatif, M.M., 2022. Fabrication, characterization, and potential application of modified sawdust sorbents for efficient removal of heavy metal ions and anionic dye from aqueous solutions. J. Clean. Prod. 332, 130021 https://doi.org/10.1016/j.jclepro.2021.130021.
Ihsanullah, I., Sajid, M., Khan, S., Bilal, M., 2022. Aerogel-based adsorbents as emerging materials for the removal of heavy metals from water: progress, challenges, and prospects. Separ. Purif. Technol. 291, 120923 https://doi.org/10.1016/j.seppur.2022.120923.
ISO 14044, 2006. Environmental Management—Life Cycle Assessment—Requirements and Guidelines (Geneva, Switzerland).
Ji, C., Xu, M., Yu, H., Lv, L., Zhang, W., 2022. Mechanistic insight into selective adsorption and easy regeneration of carboxyl-functionalized MOFs towards heavy metals. J. Hazard Mater. 424, 127684 https://doi.org/10.1016/j.jhazmat.2021.127684.
Ji, J., Chen, G., Zhao, J., 2019. Preparation and characterization of amino/thiol bifunctionalized magnetic nanoadsorbent and its application in rapid removal of Pb (II) from aqueous system. J. Hazard Mater. 368, 255–263. https://doi.org/10.1016/j.jhazmat.2019.01.035.
Joseph, L., Jun, B.-M., Flora, J.R.V., Park, C.M., Yoon, Y., 2019. Removal of heavy metals from water sources in the developing world using low-cost materials: a review. Chemosphere 229, 142–159. https://doi.org/10.1016/j.chemosphere.2019.04.198.
Katiyar, R., Patel, A.K., Nguyen, T.B., Singhania, R.R., Chen, C.W., Dong, C.D., 2021. Adsorption of copper (II) in aqueous solution using biochars derived from Ascophyllum nodosum seaweed. Bioresour. Technol. 328, 124829 https://doi.org/10.1016/j.biortech.2021.124829.
Krstić, V., Urošević, T., Pešovski, B., 2018. A review on adsorbents for treatment of water and wastewaters containing copper ions. Chem. Eng. Sci. 192, 273–287. https://doi.org/10.1016/j.ces.2018.07.022.
Kumar, V., Dwivedi, S.K., Oh, S., 2022. A critical review on lead removal from industrial wastewater: recent advances and future outlook. J. Water Proc. Eng. 45, 102518 https://doi.org/10.1016/j.jwpe.2021.102518.
Kumar, V., Pandita, S., Singh Sidhu, G.P., Sharma, A., Khanna, K., Kaur, P., Bali, A.S., Setia, R., 2021. Copper bioavailability, uptake, toxicity and tolerance in plants: a comprehensive review. Chemosphere 262, 127810. https://doi.org/10.1016/j.chemosphere.2020.127810.
Lagergren, S., 1898. About the theory of so-called adsorption of soluble substances. K. Sven. Vetenskapsakad. Handl. 24 (4), 1–39.
Langmuir, I., 1918. The adsorption of gases on plane surfaces of glass, mica and platinum. J. Am. Chem. Soc. 40, 1361–1403.
Li, W., Zhang, L., Hu, D., Yang, R., Zhang, J., Guan, Y., Lv, F., Gao, H., 2021. A mesoporous nanocellulose/sodium alginate/carboxymethyl-chitosan gel beads for efficient adsorption of Cu^{2+} and Pb^{2+}. Int. J. Biol. Macromol. 187, 922–930. https://doi.org/10.1016/j.ijbiomac.2021.07.181.
Li, X., Zhang, J., Gong, Y., Liu, Q., Yang, S., Ma, J., Zhao, L., Hou, H., 2020. Status of copper accumulation in agricultural soils across China (1985–2016). Chemosphere 244, 125516. https://doi.org/10.1016/j.chemosphere.2019.125516.
Li, X., Zhou, H., Wu, W., Wei, S., Xu, Y., Kuang, Y., 2015. Studies of heavy metal ion adsorption on Chitosan/Sulfydryl-functionalized graphene oxide composites. J. Colloid Interface Sci. 448, 389–397. https://doi.org/10.1016/j.jcis.2015.02.039.
Liang, J., He, Q., Zhao, Y., Yuan, Y., Wang, Z., Gao, Z., Hu, Z., Zhao, X., Yue, T., 2022. Synthesis of sulfhydryl modified bacterial cellulose gel membrane and its application in adsorption of patulin from apple juice. LWT 158, 113159. https://doi.org/10.1016/j.lwt.2022.113159.
Liang, X., Xu, Y., Tan, X., Wang, L., Sun, Y., Lin, D., Sun, Y., Qin, X., Wang, Q., 2013. Heavy metal adsorbents mercapto and amino functionalized palygorskite: preparation and characterization. Colloid Surf. A Physicochem. Eng. Asp. 426, 98–105. https://doi.org/10.1016/j.colsurfa.2013.03.014.
Liu, T., Liu, Q., Liu, Y., Yao, H., Zhang, Z., Wang, X., Shen, J., 2021. Fabrication of methyl acrylate modified silica aerogel for capture of Cu^{2+} from aqueous solutions. J. Sol. Gel Sci. Technol. 98, 389–400. https://doi.org/10.1007/s10971-021-05499-w.
Luo, J., Fan, C., Xiao, Z., Sun, T., Zhou, X., 2019. Novel graphene oxide/carboxymethyl chitosan aerogels via vacuum-assisted self-assembly for heavy metal adsorption capacity. Colloids Surf. A Physicochem. Eng. Asp. 578, 123584 https://doi.org/10.1016/j.colsurfa.2019.123584.
Lyu, H., Xia, S., Tang, J., Zhang, Y., Gao, B., Shen, B., 2020. Thiol-modified biochar synthesized by a facile ball-milling method for enhanced sorption of inorganic Hg^{2+} and organic CH_3Hg^+. J. Hazard Mater. 384, 121357 https://doi.org/10.1016/j.jhazmat.2019.121357.
Mitra, S., Chakraborty, A.J., Tareq, A.M., Emran, T.B., Nainu, F., Khusro, A., Idris, A.M., Khandaker, M.U., Osman, H., Alhumaydhi, F.A., Simal-Gandara, J., 2022. Impact of heavy metals on the environment and human health: novel therapeutic insights to counter the toxicity. J. King Saud Univ. Sci. 34, 101865 https://doi.org/10.1016/j.jksus.2022.101865.
Motahari, S., Heidari, B.S., Motlagh, G.H., 2015. Resorcinol formaldehyde xerogels modified with mercapto functional groups as mercury adsorbent. J. Appl. Polym. Sci. 132 (37), 42543–42555. https://doi.org/10.1002/app.42543.
Motahari, S., Nodeh, M., Maghsoudi, K., 2016. Absorption of heavy metals using resorcinol formaldehyde aerogel modified with amine groups. Desalination Water Treat. 57 (36), 16886–16897. https://doi.org/10.1080/19443994.2015.1082506.
Mirzaee, S.S., Salahi, E., Khanlarkhani, A., 2019. Kinetics, isotherms and thermodynamic modeling of Mn^{2+} and Zn^{2+} single and binary removal using mercapto functionalized silica aerogel. J. Dispersion Sci. Technol. 40 (5), 657–667. https://doi.org/10.1080/01932691.2018.1478301.
Naat, J.N., Neolaka, Y.A.B., Lapailaka, T., Tj, R.T., Sabarudin, A., Darmokoesoemo, H., Kusuma, H.S., 2021. Adsorption of Cu(II) and Pb(II) using silica@mercacapto (HS@M) hybrid adsorbent synthesized from silica of takari sand: optimization of parameters and kinetics. Rasayan J. Chem. 14, 550–560. https://doi.org/10.31788/RJC.2021.1415803.
Nuengmatcha, P., 2021. Mercapto-functionalized magnetic graphene quantum dots as adsorbent for Cd^{2+} removal from wastewater. Environ. Process. 8, 1289–1360. https://doi.org/10.1007/s40710-021-00523-1.
Nuengmatcha, P., Mahachai, R., Chanthai, S., 2015. Adsorption of functionalized thiol-graphene oxide for removal of mercury from aqueous solution. Asian J. Chem. 27, 4167–4170. https://doi.org/10.14233/ajchem.2015.19479.
Oyetade, O.A., Skelton, A.A., Nyamori, V.O., Jonnalagadda, S.B., Martincigh, B.S., 2017. Experimental and DFT studies on the selective adsorption of Pb^{2+} and Zn^{2+} from aqueous solution by nitrogen-functionalized multiwalled carbon nanotubes. Sep. Purif. 188, 174–187. https://doi.org/10.1016/j.seppur.2017.07.022.
Rehman, M., Liu, L., Wang, Q., Saleem, M.H., Bashir, S., Ullah, S., Peng, D., 2019. Copper environmental toxicology, recent advances, and future outlook: a review. Environ. Sci. Pollut. Res. 26, 18003–18016. https://doi.org/10.1007/s11356-019-05073-6.

Roginsky, S., Zeldovich, Y.B., 1934. The catalytic oxidation of carbon monoxide on manganese dioxide. Acta Phys. Chem. USSR 1, 554.

Rong, N., Chen, C., Ouyang, K., Zhang, K., Wang, X., Xu, Z., 2021. Adsorption characteristics of directional cellulose nanofiber/chitosan/montmorillonite aerogel as adsorbent for wastewater treatment. Separ. Purif. Technol. 274, 119120 https://doi.org/10.1016/j.seppur.2021.119120.

Sardarian, A.R., Kazemnejadi, M., Esmaeilpour, M., 2021. Functionalization of superparamagnetic Fe_3O_4@SiO_2 nanoparticles with a Cu(II) binuclear Schiff base complex as an efficient and reusable nanomagnetic catalyst for *N*-arylation of α-amino acids and nitrogen-containing heterocycles with aryl halides. Appl. Organomet. Chem. 35 (1), 6051. https://doi.org/10.1002/aoc.6051.

Sellaoui, L., Mendoza-Castillo, D.I., Reynel-Ávila, H.E., Ávila-Camacho, B.A., Díaz-Muñoz, L.L., Ghalla, H., Bonilla-Petriciolet, A., Lamine, A.B., 2019. Understanding the adsorption of Pb^{2+}, Hg^{2+} and Zn^{2+} from aqueous solution on a lignocellulosic biomass char using advanced statistical physics models and density functional theory simulations. Chem. Eng. J. 365, 305–316. https://doi.org/10.1016/j.cej.2019.02.052.

Sert Çok, S., Koç, F., Gizli, N., 2021. Lightweight and highly hydrophobic silica aerogels dried in ambient pressure for an efficient oil/organic solvent adsorption. J. Hazard Mater. 408, 124858 https://doi.org/10.1016/j.jhazmat.2020.124858.

Štandeker, S., Veronovski, A., Novak, Z., Knez, Ž., 2011. Silica aerogels modified with mercapto functional groups used for Cu(II) and Hg(II) removal from aqueous solutions. Desalination 269, 223–230. https://doi.org/10.1016/j.desal.2010.10.064.

Sun, H., Ji, Z., He, Y., Wang, L., Zhan, J., Chen, L., Zhao, Y., 2022. Preparation of PAMAM modified PVDF membrane and its adsorption performance for copper ions. Environ. Res. 204, 111943 https://doi.org/10.1016/j.envres.2021.111943.

Swaringen, B.F., Gawlik, E., Kamenov, G.D., McTigue, N.E., Cornwell, D.A., Bonzongo, J. C.J., 2022. Children's exposure to environmental lead: a review of potential sources, blood levels, and methods used to reduce exposure. Environ. Res., 112025 https://doi.org/10.1016/j.envres.2021.112025.

Tahir, M.U., Su, X., Zhao, M., Liao, Y., Wu, R., Chen, D., 2019. Preparation of hydroxypropyl-cyclodextrin-graphene/Fe_3O_4 and its adsorption properties for heavy metals. Surface. Interfac. 16, 43–49. https://doi.org/10.1016/j.surfin.2019.04.007.

Tang, C., Brodie, P., Li, Y., Grishkewich, N.J., Brunsting, M., Tam, K.C., 2020. Shape recoverable and mechanically robust cellulose aerogel beads for efficient removal of copper ions. Chem. Eng. J. 392, 124821 https://doi.org/10.1016/j.cej.2020.124821.

Tang, J., Chen, Y., Zhao, M., Wang, S., Zhang, L., 2021. Phenylthiosemicarbazide-functionalized UiO-66-NH_2 as highly efficient adsorbent for the selective removal of lead from aqueous solutions. J. Hazard Mater. 413, 125278 https://doi.org/10.1016/j.jhazmat.2021.125278.

Tempkin, M.I., Pyzhev, V.J.A.P.C., 1940. Kinetics of ammonia synthesis on promoted iron catalyst. Acta Phys. Chim. USSR 12 (1), 327.

Tran, H.N., You, S.J., Hosseini-Bandegharaei, A., Chao, H.P., 2017. Mistakes and inconsistencies regarding adsorption of contaminants from aqueous solutions: a critical review. Water Res. 120, 88–116. https://doi.org/10.1016/j.watres.2017.04.014.

Vareda, J.P., Durães, L., 2019. Efficient adsorption of multiple heavy metals with tailored silica aerogel-like materials. Environ. Technol. 40, 529–541. https://doi.org/10.1080/09593330.2017.1397766.

Wang, B., Bai, Z., Jiang, H., Prinsen, P., Luque, R., Zhao, S., Xuan, J., 2019a. Selective heavy metal removal and water purification by microfluidically-generated chitosan microspheres: characteristics, modeling and application. J. Hazard Mater. 364, 192–205. https://doi.org/10.1016/j.jhazmat.2018.10.024.

Wang, B., Xuan, J., Yang, X., Bai, Z., 2021a. Synergistic DFT-guided design and microfluidic synthesis of high-performance ion-imprinted biosorbents for selective heavy metal removal. Colloid Surf. A Physicochem. Eng. Asp. 626, 127030 https://doi.org/10.1016/j.colsurfa.2021.127030.

Wang, C., Yang, Z., Song, W., Zhong, Y., Sun, M., Gan, T., Bao, B., 2021b. Quantifying gel properties of industrial waste-based geopolymers and their application in Pb^{2+} and Cu^{2+} removal. J. Clean. Prod. 315, 128203 https://doi.org/10.1016/j.jclepro.2021.128203.

Wang, L., Xu, W.-H., Yang, R., Zhou, T., Hou, D., Zheng, X., Liu, J.-H., Huang, X.-J., 2013. Electrochemical and density functional theory investigation on high selectivity and sensitivity of exfoliated nano-zirconium phosphate toward lead(II). Anal. Chem. 85, 3984–3990. https://doi.org/10.1021/ac3037014.

Wang, M., Yang, Q., Zhao, X., Wang, Z., 2019b. Highly efficient removal of copper ions from water by using a novel alginate-polyethyleneimine hybrid aerogel. Int. J. Biol. Macromol. 138, 1079–1086. https://doi.org/10.1016/j.ijbiomac.2019.07.160.

Wang, Z., Tu, Q., Sim, A., Yu, J., Duan, Y., Poon, S., Liu, B., Han, Q., Urban, J.J., Sedlak, D., Mi, B., 2020. Superselective removal of lead from water by two-dimensional MoS_2 nanosheets and layer-stacked membranes. Environ. Sci. Technol. 54, 12602–12611. https://doi.org/10.1021/acs.est.0c02651.

Weber Jr., W.J., Morris, J.C., 1963. Kinetics of adsorption on carbon from solution. J. Sanit. Eng. Div. 89 (2), 31–59. https://doi.org/10.1061/JSEDAI.0000430.

Wei, N., Yang, J., Dong, K., Fang, Y., Qin, Z., 2022. Amino-functionalized bovine serum albumin amyloid fibrils aerogel for absorbing copper from water. J. Clean. Prod. 380, 134955 https://doi.org/10.1016/j.jclepro.2022.134955.

Xu, L., Liu, Y., Wang, J., Tang, Y., Zhang, Z., 2021. Selective adsorption of Pb^{2+} and Cu^{2+} on amino-modified attapulgite: kinetic, thermal dynamic and DFT studies. J. Hazard Mater. 404, 124140 https://doi.org/10.1016/j.jhazmat.2020.124140.

Yadav, S., Asthana, A., Singh, A.K., Chakraborty, R., Vidya, S.S., Susan, M.A.B.H., Carabineiro, S.A.C., 2021. Adsorption of cationic dyes, drugs and metal from aqueous solutions using a polymer composite of magnetic/β-cyclodextrin/activated charcoal/Na alginate: isotherm, kinetics and regeneration studies. J. Hazard Mater. 409, 124840 https://doi.org/10.1016/j.jhazmat.2020.124840.

Yang, X., Wei, Y., Jiang, Y., Wang, Y., Chen, L., Peng, L., Zhang, S., Yan, Y., Yan, Y., 2021. High efficiency phosphate removal was achieved by lanthanum-modified mesoporous silica aerogels with cellulose-guided templates. Ind. Eng. Chem. Res. 60, 5352–5363. https://doi.org/10.1021/acs.iecr.0c05590.

Zhang, J., Wang, Y., Liang, D., Xiao, Z., Xie, Y., Li, J., 2020. Sulfhydryl modified chitosan aerogel for the adsorption of heavy metal ions and organic dyes. Ind. Eng. Chem. Res. 59 (32), 14531–14536. https://doi.org/10.1021/acs.iecr.0c02317.

Zhang, J., Li, T., Li, X., Liu, Y., Li, N., Wang, Y., Li, X., 2021. A key role of inner-cation-π interaction in adsorption of Pb(II) on carbon nanotubes: experimental and DFT studies. J. Hazard Mater. 412, 125187 https://doi.org/10.1016/j.jhazmat.2021.125187.

Zhu, S., Khan, M.A., Kameda, T., Xu, H., Wang, F., Xia, M., Yoshioka, T., 2022. New insights into the capture performance and mechanism of hazardous metals Cr^{3+} and Cd^{2+} onto an effective layered double hydroxide based material. J. Hazard Mater. 426, 128062 https://doi.org/10.1016/j.jhazmat.2021.128062.

Zhu, Y., Lin, H., Feng, Q., Zhao, B., Lan, W., Li, T., Xue, B., Li, M., Zhang, Z., 2021. Sulfhydryl-modified SiO_2 cryogel: a pH-insensitive and selective adsorbent for efficient removal of mercury in waters. Colloids Surf. A Physicochem. Eng. Asp. 617, 126382 https://doi.org/10.1016/j.colsurfa.2021.126382.